nature biomedical engineering

Article

https://doi.org/10.1038/s41551-025-01596-1

Small intracellular vesicles outperform small extracellular vesicles in uptake, drug delivery and retinal neuroprotection

Received: 29 July 2024

Accepted: 2 December 2025

Published online: 13 January 2026

Check for updates

Hui Zhang[1], Xinyue Yu[1], Fuhua Yang[1], Jinying An[1], Lin Su[1], Yuqing Liu[1], Mi Zhang[1], Ruiyan Fan[1], Hongli Yang[1], Xiaorong Li[1] ✉ & Xiaomin Zhang[1,2] ✉

Small extracellular vesicles have been widely studied for their therapeutic properties and ability to deliver bioactive molecules. In addition to secretory vesicles, cells contain small intracellular vesicles involved in physiological and metabolic processes, whose therapeutic potential remains unexplored. Here we developed protocols to isolate small intracellular vesicles from multiple cell types and systematically compared their molecular and functional profiles to extracellular vesicles. Intracellular vesicles are smaller, yield higher quantities and demonstrate enhanced cellular uptake in both in vitro and in vivo models. Molecular profiling revealed that intracellular vesicles are enriched in proteins associated with the endoplasmic reticulum and Golgi apparatus, possess distinct microRNA signatures linked to intracellular membrane systems, and contain elevated levels of phospholipids such as phosphatidylcholine and phosphatidylethanolamine. Vesicles derived from umbilical cord mesenchymal stem cells showed superior therapeutic efficacy in a model of retinal degeneration by reducing endoplasmic reticulum stress and delivering neuroprotective factors. In addition, intracellular vesicles exhibited enhanced drug-loading capacity and efficient delivery of lipophilic compounds to the retina. These findings position intracellular vesicles as promising candidates for therapeutic applications.

Exosomes are small extracellular vesicles (sEVs) of endosomal origin. They are 30–150 nm in diameter and are formed through intraluminal vesicle budding within multivesicular bodies[1]. sEVs selectively package proteins, RNAs, metabolites and lipids, which can be transferred to recipient cells and are crucial to intercellular communication in normal and disease states[2–4]. Owing to their biological properties, exosome-based approaches have been extensively explored to discover diagnostic biomarkers and establish therapeutic strategies[1,5,6]. However, many challenges remain for their industrial and clinical translation as therapeutic products, including limited production, potential contamination, instability and low therapeutic efficacy. Therefore, numerous studies have focused on developing alternatives to sEVs, such as engineered vesicles obtained by extruding red blood cell membranes and artificial cell-derived vesicles generated by repeated freeze–thaw cycles[7–9]. These engineered vesicles and sEVs exhibit great versatility and have been widely employed in various drug delivery strategies[10,11]. However, compared to naturally occurring vesicles (such as apoptotic vesicles and exosomes), the inherent roles of these vesicles themselves have not been well elucidated, and the engineering process may be accompanied by altered biological functions or reduced effectiveness.

Intracellularly, numerous nanosized intrinsic vesicles freely move between membrane-enriched organelles and facilitate intracellular

[1]Tianjin Key Laboratory of Retinal Functions and Diseases, Tianjin Branch of National Clinical Research Center for Ocular Disease, Eye Institute and School of Optometry, Tianjin Medical University Eye Hospital, Tianjin, China. [2]Tianjin Eye Hospital, Tianjin Key Laboratory of Ophthalmology and Visual Science, Tianjin Eye Institute, Nankai University Affiliate Tianjin Eye Hospital; Clinial College of Ophthalmology, Tianjin Medical University, Tianjin, China. ✉e-mail: lixiaorong@tmu.edu.cn; xzhang08@tmu.edu.cn

material transport and cellular secretion pathways[12–14]. Generated via vesicle budding, intracellular vesicles can arise from multiple organelles, such as the endoplasmic reticulum (ER), Golgi apparatus, plasma membrane and endosomes[13,15–20]. They comprise diverse groups of membrane-bound particles, such as constitutive secretory vesicles[20], synaptic vesicles[13], COP-coated vesicles[18,21], Golgi-derived vesicles[19], clathrin-coated vesicles[22], and transport vesicles between the ER and Golgi apparatus[23]. These vesicles are important components of the cellular transport system capable of immediate cargo delivery of proteins, RNAs and lipids, showing potential for modulating overall cellular function.

Although the intracellular functions of intracellular vesicles have been widely investigated, their isolation and further application in biomedical engineering have not yet been explored. Therefore, in this study, we developed protocols to isolate intracellular vesicles from different cell types. Due to the small size of these separated vesicles, we term them small intracellular vesicles (sIVs). sIVs are smaller than sEVs, with simpler isolation methods, higher yield, distinct molecular profiles and enhanced drug delivery. We also investigated their biological characteristics and potential therapeutic applications. Umbilical cord mesenchymal stem cell (MSC)-derived sIVs more effectively alleviated retinal degeneration by reducing ER stress and providing neuroprotective factors. This study presents sIVs as superior alternatives to conventional biological nanovesicles for clinical translation.

Results

sIVs are smaller, with a higher yield and greater stability at physiological temperature than sEVs

A flowchart for the collection of sIVs and sEVs is illustrated in Fig. 1a. Transmission electron microscope (TEM) and cryogenic electron microscopy (cryo-EM) analysis of isolated sEVs and sIVs from three cell types—MSCs, 293T and HeLa—showed characteristic cup morphology with a lipid bilayer (Fig. 1b, and Supplementary Figs. 1, 2a and 3a). The particle size distribution verified by nanoparticle tracing analysis confirmed that sIVs are smaller than sEVs (Fig. 1c–e, and Supplementary Figs. 2b,c and 3b,c). The isolation of sEVs requires a 48-h secretion period, followed by 190 min of centrifugation. In contrast, sIVs only necessitate 30 s of ultrasonication and 110 min of centrifugation. This reduces the processing time by 58% while increasing vesicle yield by 20- to 40-fold (Fig. 1f, and Supplementary Figs. 2d and 3d). The protein content in sIVs derived from 1×10^7 cells was 5- to 10-fold higher than that in sEVs (Fig. 1g, and Supplementary Figs. 2e and 3e). Coomassie brilliant blue staining revealed different protein components in sEVs and sIVs (Fig. 1h, and Supplementary Figs. 2f and 3f). In addition, sEVs from the three cell types expressed all typical exosome markers, including ALG-2-interacting protein X (Alix), heat shock protein 70 (HSP70), tumour susceptibility gene 101 (TSG101) and CD63, as well as endosomal markers such as Rab7 and early endosome antigen 1 (EEA1), whereas sIVs expressed them at low levels or not at all (Fig. 1i, and Supplementary Figs. 2g and 3g). Hence, sIVs are smaller, higher-yield vesicles than sEVs; their different protein composition, characterized by minimal expression of canonical exosome markers and endosome markers, suggests different origins for sIVs vs sEVs.

To evaluate the stability of the vesicles at different temperatures, suspensions of sEVs and sIVs from three cell types were equally divided into three parts and stored at different temperatures (−80, 4 and 37 °C). After 24 h, the morphology, size and protein contents were evaluated. Both vesicles were stable at −80 and 4 °C. However, the morphology of sEVs was significantly damaged at 37 °C, with an irregular shape, broken vesicles and rough borders (Fig. 1j, and Supplementary Figs. 2h and 3h), and the number of sEVs was also decreased (Fig. 1k, and Supplementary Figs. 2i and 3i). In contrast, sIVs maintained stable morphology and particle numbers at 37 °C. Thus, sIVs were deemed more stable at physiological temperatures than sEVs.

sIVs densely disperse within cells without being released into extracellular space

To gain additional insights into the intracellular localization of sIVs, we identified marker proteins differentially expressed between sIVs and sEVs through proteomic analysis, followed by intracellular staining. By examining the intersection of proteins from these three sources, we identified 106 commonly expressed proteins across the three cell types (Supplementary Fig. 4a and Table 1) and ranked their expression from high to low in the different cell types (Supplementary Fig. 4b–d). Transmembrane protein 214 (TMEM214) exhibited the highest expression in MSCs and ranked within the top 50 in the other two cell types. Western blot analysis confirmed that TMEM214 was expressed by sIVs but not by sEVs (Supplementary Fig. 4e). TMEM214 is a transmembrane protein involved in several cellular processes, such as vesicle trafficking and protein transport[24]. Immunogold labelling coupled with TEM clearly revealed TMEM214 localization on the surface of sIVs (Supplementary Fig. 4f). Consequently, we labelled TMEM214 with mCherry to visualize the intracellular status of sIVs, whereas GFP-labelled CD63 was utilized as a marker for late endosomes, multivesicular bodies and sEVs[25–27].

Total internal reflection fluorescence structured illumination microscopy (TIRF-SIM) enables the assessment of vesicle dynamics at or near the plasma membrane with high spatiotemporal resolution. CD63 was uniformly distributed on the cytomembrane, whereas TMEM214 was absent (Fig. 1l). This ruled out the possibility that sIVs originate from plasma membrane reorganization. Next, we performed time-lapse wide-field imaging to observe dynamic changes of CD63- and TMEM214-labelled structures in living cells (Supplementary Videos 1–3). CD63-labelled particles were relatively large, with some displaying vesicular-like granules. A few small CD63-labelled particles were noted in the extracellular space. We tracked the secretion of one sEV from the cell membrane (Fig. 1m, white arrowheads). TMEM214-labelled structures moved within the cell without being released. It was difficult to distinguish their particle shape due to their small size. In these images and videos, CD63-labelled vesicles were considered multivesicular bodies with a large diameter and intraluminal vesicle; the small released particles might have been exosomes, whereas the cloud-like TMEM214-labelled structures should be densely distributed sIVs. These results suggest that the isolated sIVs only contain inherent nanovesicles in the cells, excluding large multivesicular bodies.

To further investigate the intracellular status of these nanovesicles, we performed thin-section TEM analysis on three cell types (Supplementary Fig. 5a). As Brefeldin A (BFA) impairs intracellular vesicle formation and transport[28], we investigated the effect of BFA on the morphology and quantity of sIVs. The results revealed that, in the absence of BFA treatment, intracellular vesicles labelled with TMEM214 immunogold exhibited intact membrane structures and diameters smaller than 100 nm. However, BFA stimulation damaged the structure of sIVs in all three cell types, resulting in larger vacuoles, and TMEM214 showed a more diffuse intracellular distribution (Supplementary Fig. 5a). The BFA-treated group exhibited decreased quantity and content of sIVs (Supplementary Figs. 5b–g), suggesting that sIVs comprise an intracellular vesicle pool involved in vesicle transport events within the cells. Therefore, sIVs are endogenous nanovesicles (30–100 nm in diameter) with bilayer lipid membranes naturally present in cells, characterized by TMEM214 expression.

sIVs comprise a mixture of nanovesicles involved in intracellular material transport with intracellular biological functions

To characterize the protein composition of sIVs, we conducted proteomic profiling of sIVs and sEVs using label-free mass spectrometry. Pearson analysis revealed slight intragroup variability in MSC-sIVs across donors compared to pronounced sIV–sEV differences (Supplementary Fig. 6a). This pattern was consistent in 293T and HeLa cell-derived vesicles (Supplementary Fig. 6b,c). The Venn diagram

https://doi.org/10.1038/s41551-025-01596-1

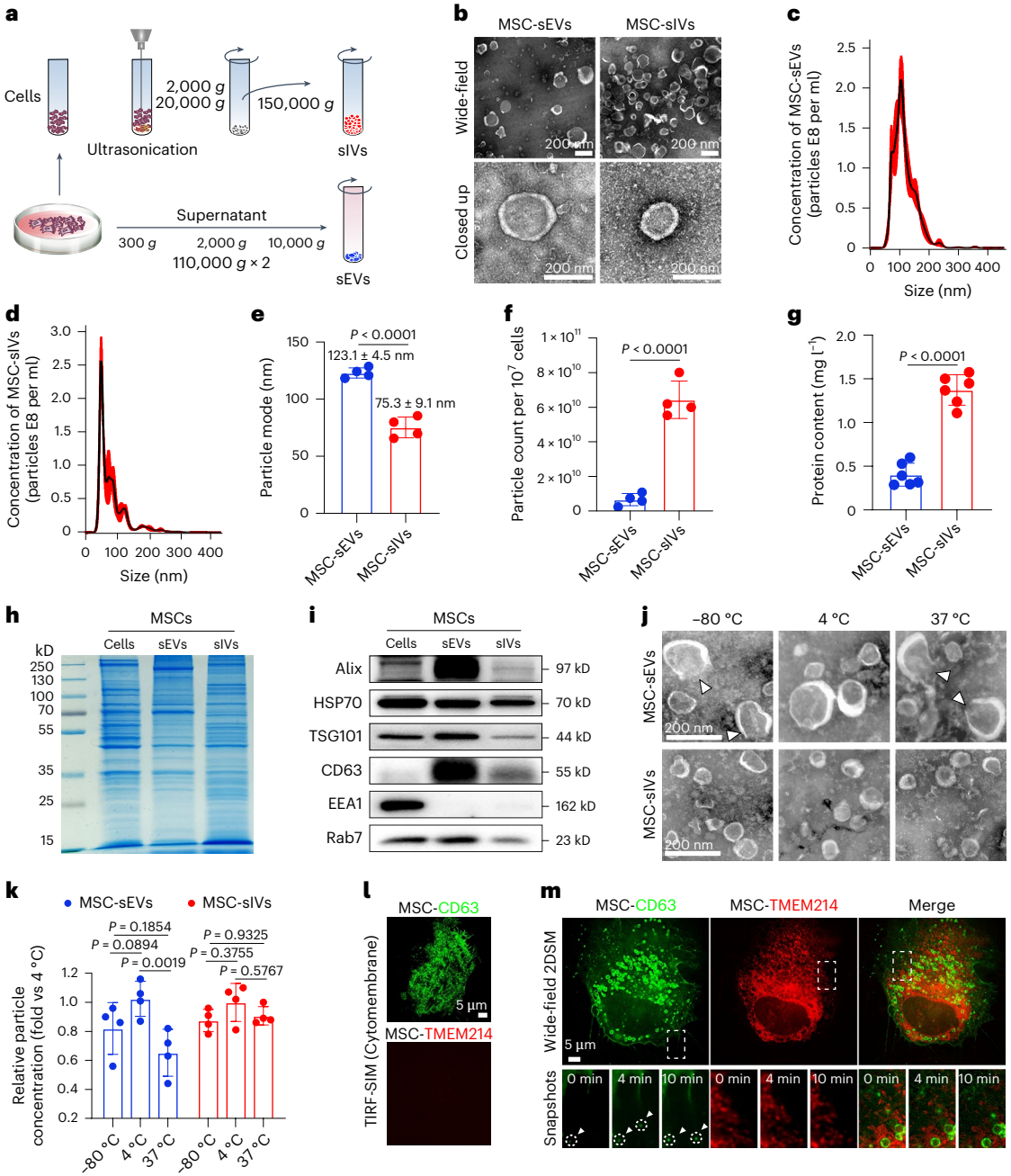

Fig. 1 | Characterization of sEVs and sIVs derived from MSCs. a, Flowchart of the collection process for sIVs and sEVs. **b**, TEM images of sEVs and sIVs stained with phosphotungstic acid. **c**, Nanoparticle tracking analysis, showing particle size distribution of sEVs. **d**, Nanoparticle tracking analysis, showing particle size distribution of sIVs. **e**, Average sizes of sEVs and sIVs ($n = 4$). **f**, Nanoparticle tracking analysis of particle count in sEVs and sIVs derived from 10^7 MSCs ($n = 4$). **g**, Protein content of sEVs and sIVs derived from 10^7 MSCs via protein quantification ($n = 6$). Two-tailed unpaired Student's t-test. **h**, Protein bands of MSCs, sEVs and sIVs visualized with Coomassie brilliant blue. **i**, Western blotting analysis of MSCs, sEVs and sIVs. Equal protein loading was used as a blotting control. Alix, HSP70, TSG101 and CD63 are exosome markers. EEA1 and Rab7 are endosome markers. **j**, TEM images of sEVs and sIVs at different temperatures (−80, 4 and 37 °C) stained with phosphotungstic acid. White arrowheads indicate damaged vesicles. **k**, Nanoparticle tracking analysis of concentration changes for sEVs and sIVs at different temperatures (−80, 4 and 37 °C) ($n = 4$). **l**, Images acquired by super-resolution microscopy with TIRF-SIM show the expression of CD63 (green) and TMEM214 (red) on the cytomembrane. **m**, Wide-field 2DSM images of the presence of CD63 (green) and TMEM214 (red) in the whole cell. Snapshots captured during 10-min dynamic observation. White arrowheads indicate the cell-shed extracellular vesicles. All n values indicate independent biological replicates yielding comparable results. Data in **e**–**g** and **k** are expressed as mean ± s.e.m. and analysed using two-tailed unpaired Student's t-test (**e**–**g**) or two-way ANOVA (**k**). The schematic in **a** was drawn using pictures from Biovisart (https://biovisart.com.cn).

in Fig. 2a demonstrates the protein contents of the cells, sEVs and sIVs. The PCA plot (Fig. 2b) shows that sEVs and sIVs exhibited distinct protein distribution patterns. Statistical analysis revealed 1,245 differentially expressed proteins between sEVs and sIVs in MSC cells, 1,841 in 293T cells and 1,474 in HeLa cells (Supplementary Fig. 7).

The protein profiles of sEVs and sIVs showed significant variations in both upregulated and downregulated proteins across different cell types. Cytomembrane-associated proteins (Annexin A6 [ANXA6] and Annexin A5 [ANXA5]) exhibited lower expression levels in sIVs than in sEVs, whereas ER and ribosome-related proteins (target of

https://doi.org/10.1038/s41551-025-01596-1

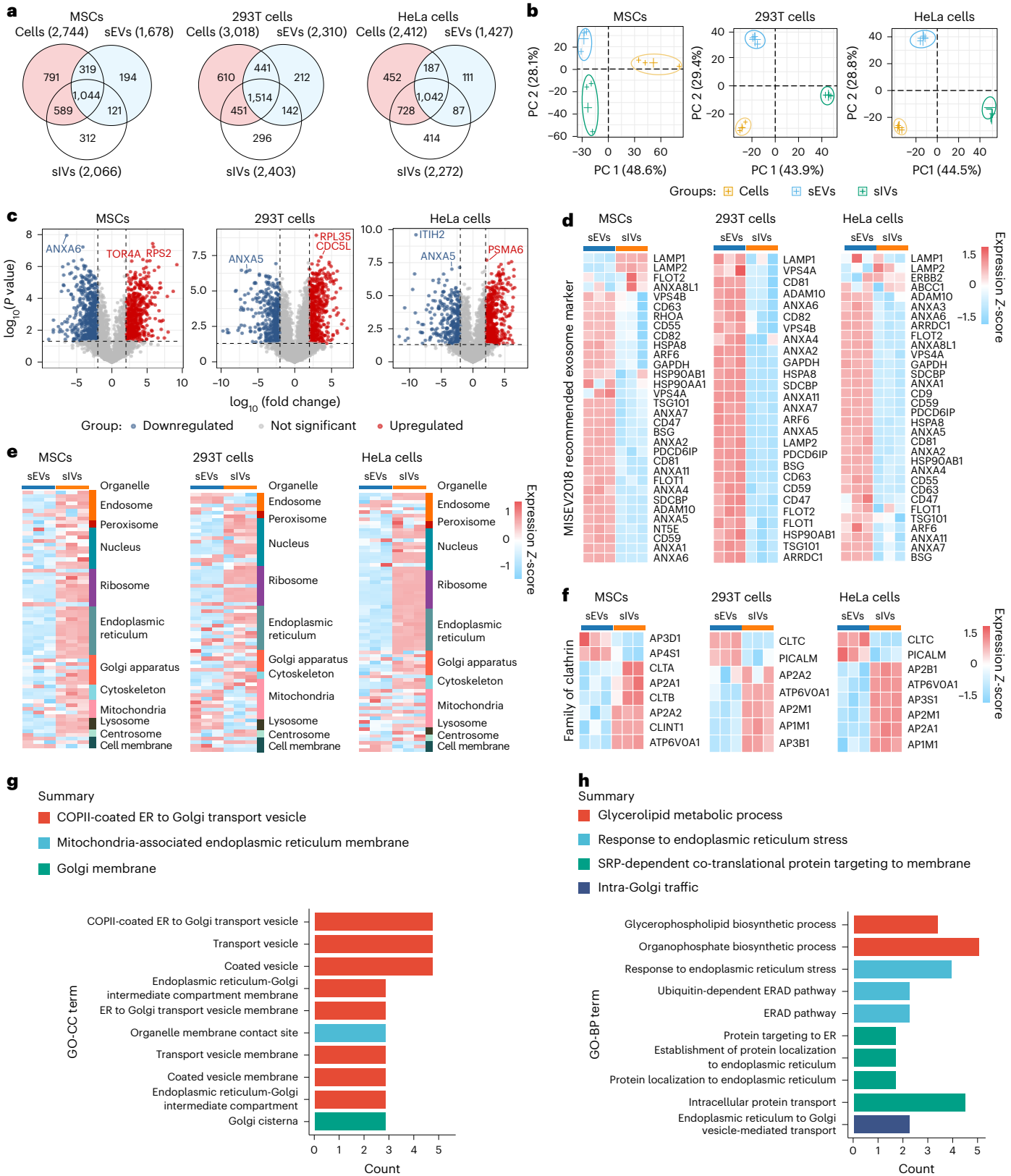

Fig. 2 | Proteomic analysis of sIVs and sEVs. a, Venn diagram of proteins identified in sIVs, sEVs and cells from MSCs, 293T and HeLa cells. **b**, Principal component analysis of normalized proteomic mass spectrometry datasets from MSCs, 293T cells and HeLa cells. **c**, Volcano plots indicating differentially expressed proteins between sEVs and sIVs from MSCs, 293T cells and HeLa cells. Two-tailed unpaired Student's *t*-test was used for the comparisons. **d**, Heat map demonstrating the differential expression of exosomal markers between sEVs and sIVs from MSCs, 293T cells and HeLa cells. **e**, Heat map demonstrating the differential expression of organelle markers between sEVs and sIVs from MSCs, 293T cells and HeLa cells. **f**, Heat map of normalized spectral counts for the clathrin protein family in sEVs and sIVs from MSCs, 293T cells and HeLa cells. **g**, Gene ontology-cellular component (GO-CC) enrichment analysis for 106 co-expressed unique proteins in sIVs of MSCs, 293T cells and HeLa cells. **h**, Gene ontology-biological process (GO-BP) enrichment analysis for 106 co-expressed unique proteins in sIVs of MSCs, 293T cells and HeLa cells.

rapamycin 4A [TOR4A] and ribosomal protein S2 [RPS2]) were upregulated in sIVs (Fig. 2c). We further assessed exosome marker expression in sEVs vs sIVs, as recommended by the MISEV2018 guidelines[29]. We confirmed that sEVs exhibited higher expression levels of exosome markers, whereas sIVs demonstrated lower expression levels of most of the markers (Fig. 2d). Moreover, sIVs harboured a higher amount of intracellular organelle proteins than sEVs, with elevated expression levels of proteins associated with membrane-enriched organelles (for example, ER and Golgi apparatus). In contrast, sEVs contained more abundant cytomembrane proteins (Fig. 2e). The clathrin protein family facilitates the formation of small vesicles in the cytoplasm and is involved in multiple membrane trafficking pathways[30]. Notably, sIVs exhibited pronounced upregulation of most clathrin proteins, whereas sEVs presented the reverse pattern (Fig. 2f).

Gene enrichment analysis was performed on 106 proteins only expressed in sIVs and co-expressed among sIVs from the three cell types. In terms of cellular component (CC), these proteins were associated with COPII-coated ER to Golgi transport vesicle, transport vesicle, coated vesicle, ER to Golgi transport vesicle membrane, ER–Golgi intermediate compartment, transport vesicle membrane and coated vesicle membrane (Fig. 2g). The enriched biological processes (BP) included the glycerophospholipid biosynthetic process, response to ER stress, ubiquitin-dependent ER-associated degradation pathway, intracellular protein transport and ER to Golgi vesicle-mediated transport (Fig. 2h). On the basis of these findings, sIVs are defined as a mixture of intracellular vesicles that mediate protein secretion and material transport across organelles. They are distinct from and should not be mistaken for artefacts derived from cell lysates, extracellular vesicle precursors or fragments.

The distinct miRNA profiles of sEVs and sIVs demonstrate that sIVs are closely associated with intracellular membrane-like organelles

Small RNA (sRNA) sequencing was conducted for sEVs and sIVs isolated from the three cell types. There was no significant difference in the abundance of sRNAs in sEVs and sIVs (Fig. 3a). Pearson analysis revealed slight intragroup variability in MSC-sIVs across donors compared to pronounced sIV–sEV differences, as well as in 293T cells and HeLa cells (Supplementary Fig. 8a). Among the sRNA populations, micro-RNAs (miRNAs) constituted the major component in sIVs, whereas YRNA represented the most common sRNA component in sEVs (Fig. 3b); MSC-sIVs contained the highest relative levels of miRNAs (92.52%). Since miRNAs have extensive biological regulatory functions and occupy a large proportion of sRNAs in sIVs, we conducted further analysis using a Venn diagram and principal component analysis (PCA). Although sEVs and sIVs contained overlapping miRNAs (Fig. 3c), significant differences were observed in the miRNA components (Fig. 3d). By analysing the highly abundant miRNAs (Fig. 3e and Supplementary Fig. 8b) and differentially expressed miRNAs (Supplementary Fig. 8c) in sEVs and sIVs, we found that sIVs were enriched for miRNAs implicated in intracellular regulatory processes, a pattern not observed in sEVs. We performed Gene Ontology (GO) enrichment on the predicted targets of miRNAs showing differential expression between MSC-sIVs and MSC-sEVs, which were associated with intracellular metabolic processes, localization to membrane-related organelles and enzymatic metabolic reactions. (Fig. 3f). Results of Kyoto Encyclopedia of Genes and Genomes (KEGG) pathway analysis identified axon guidance (neuronal development), cell differentiation and endocytosis as enriched pathways (Fig. 3g). The GO analysis results for 293T cells and HeLa cells similarly indicated that the candidate target genes of sEVs and sIVs are related to intracellular processes, cell membranes, inner membrane systems and organelle membranes (Supplementary Figs. 9a,b). The candidate target genes in 293T cells were associated with various signalling pathways, such as cAMP and Ras (Supplementary Fig. 9c). In contrast, in HeLa cells, the candidate target genes were associated with neuronal synapse and MAPK signalling pathways (Supplementary Fig. 9d). In summary, the miRNA compositions of sEVs and sIVs differ, with miRNA in sIVs closely associated with intracellular membrane-like organelles and participating in intracellular processes.

sEVs and sIVs exhibit distinct lipid characteristics

Since we performed untargeted lipid profiling, a broad range of lipids were identified in the vesicles from MSCs, 293T cells and HeLa cells. In all vesicles, the proportions of phosphatidylcholine (PC) and phosphatidylethanolamine (PE) were relatively higher than those of other lipids (Extended Data Fig. 1a–c), as they are the main components of biological membranes. PCA demonstrated different and distinct lipid distribution patterns between sEVs and sIVs of the three cell types (Extended Data Fig. 1d–f). The lipidomic bar chart, drawn using all metabolites, displays the relative abundance percentage changes of different lipids in sIVs and sEVs (Extended Data Fig. 2). In MSCs, glycerophospholipids, such as PC, phosphatidylinositol (PI) and PE, were upregulated in sIVs, with PC exhibiting the highest relative difference in sIVs compared with sEVs (Extended Data Fig. 2a). In 293T cells, phospholipids, such as PE and PI, were significantly upregulated in sIVs, with PE exhibiting the highest relative difference compared with sEVs (Extended Data Fig. 2b). In HeLa cells, sulfatide hexosylceramide (SHexCer), PI and sphingomyelin were significantly upregulated in sIVs, with SHexCer exhibiting the highest relative difference compared with sEVs (Extended Data Fig. 2c). Therefore, the differences in various lipid compositions can differentiate sIVs from sEVs.

MSC-sIVs more effectively rescue retinal structure and function than MSC-sEVs in light-induced injury models

Blue-light exposure can lead to retinal damage, primarily characterized by thinning and decreased electrophysiological function[31]. To investigate the potential therapeutic effects of MSC-derived vesicles on retinal damage, we treated blue-light-induced retinal injury with MSC-sEVs and MSC-sIVs. Retinal thickness was significantly reduced on optical coherence tomography (OCT) following blue-light exposure (Fig. 4a,b), whereas high doses of MSC-sEVs and MSC-sIVs significantly ameliorated the thinning of the retina (Fig. 4c). Haematoxylin and eosin (H&E) staining on eye sections collected 7 days after blue-light induction showed significant deterioration in the outer retinal layers (Fig. 4d,e). MSC-sIVs, especially at higher doses, demonstrated a superior rescuing effect compared with MSC-sEVs in terms of reducing the loss of nuclei in the outer nuclear layer (ONL) (Fig. 4d,e). Blue light can also exert phototoxic effects on retinal ganglion cells (RGCs)[32]. Flat-mounted retinas were divided into central, intermediate and peripheral zones, and RGCs marked by RNA-binding protein with multiple splicing (RBPMS) were counted using ImageJ (Extended Data Fig. 3a–c)[33]. Reduced RGC abundance was observed in the middle and peripheral zones in PBS-treated mice, without significant differences in the central retinal region among groups (Extended Data Fig. 3d–f). MSC-sIVs rescued cell loss in the middle and peripheral zones, whereas sIVs exhibited a more protective effect in the peripheral zone compared with sEVs at the same dose (Extended Data Fig. 3e,f). Electroretinography (ERG) *a*- and *b*-wave responses were significantly diminished in PBS-treated mice at 5 days post blue-light exposure, whereas MSC-sIVs and MSC-sEVs partially restored retinal function, with MSC-sIVs exhibiting a better therapeutic effect than MSC-sEVs (Fig. 4f,g). Hence, MSC-sIVs are superior to MSC-sEVs in rescuing the retinal structure and function from blue-light-induced retinal injury.

Since rhodopsin is a functional biomarker of rod photoreceptors, we stained the retina sections with an anti-rhodopsin antibody and found reduced accumulation of rhodopsin in the ONL of the PBS-treated mice retina; however, MSC-sEVs and MSC-sIVs reversed this decrease (Fig. 4h). High-dose MSC-sIV treatment demonstrated the strongest therapeutic efficacy and exhibited a significantly superior effect compared with an equivalent MSC-sEV dose (Fig. 4i and

https://doi.org/10.1038/s41551-025-01596-1

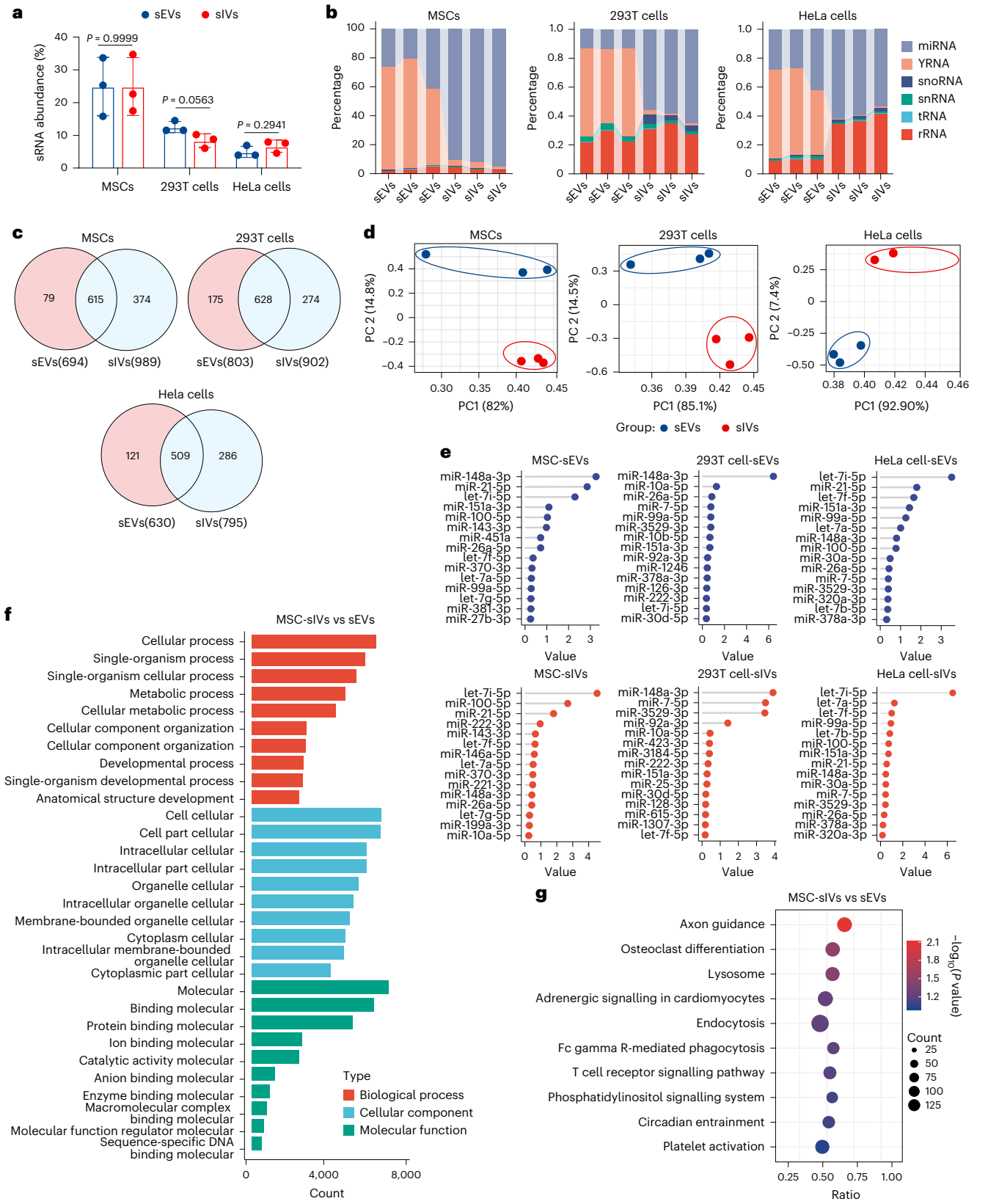

Fig. 3 | RNA expressions of sIVs and sEVs. a, Small RNA abundance in sEVs and sIVs obtained from MSCs, 293T cells and HeLa cells ($n = 3$ biologically independent samples) **b**, Percentage of sRNA reads mapped to small non-coding RNA for sEVs and sIVs from MSCs, 293T cells and HeLa cells (miRNA, microRNA; snoRNA, small nucleolar RNA; snRNA, small nuclear RNA; tRNA, transfer RNA; rRNA, ribosomal RNA). **c**, Venn diagram for miRNAs identified in sIVs, sEVs and cells from MSCs, 293T cells and HeLa cells. **d**, PCA of miRNA datasets from MSCs, 293T cells and HeLa cells. **e**, Matchstick plot displaying the top 10 high-abundance miRNAs in sEVs and sIVs obtained from MSCs, 293T cells and HeLa cells. **f**, GO enrichment analysis of target genes for differentially expressed miRNAs between MSC-sIVs and MSC-sEVs. **g**, Target gene KEGG enrichment analysis for miRNAs that are differently expressed in MSC-sEVs and MSC-sIVs. Data are presented as mean ± s.e.m. Two-tailed unpaired Student's *t*-test was used for the comparisons in **a**.

Supplementary Fig. 10). These results suggest that MSC-sIV treatment, compared with MSC-sEV treatment, can better inhibit photoreceptor damage in retinal injury caused by blue light.

Retinas of PBS-treated mice exhibited high levels of apoptotic signals, primarily concentrated in the ONL, whereas mice treated with MSC-sEVs and MSC-sIVs displayed reduced apoptotic signals, with the high-dose MSC-sIV group demonstrating the most significant reduction (Fig. 4j,k). Furthermore, after light exposure, the abundance of apoptosis-related proteins, including cleaved caspase3 and Bax, was upregulated (Supplementary Fig. 11), which aligns with previous findings from western blot analyses in light-damage models[34,35]. High-dose MSC-sIVs reduced these pro-apoptotic markers and elevated B-cell lymphoma 2 (BCL-2) expression more effectively than MSC-sEVs (Supplementary Fig. 11). These results suggest that MSC-sIVs can rescue photoreceptors from apoptosis.

Exposure to intense blue light can lead to oxidative stress and inflammation, activating gliosis within the retina and leading to retinal cell death[36,37]. Glial fibrillary acidic protein (GFAP) and ionized calcium-binding adapter molecule 1 (IBA1) serve as markers for activated Müller cells and microglia, respectively. GFAP expression was markedly upregulated in the retinas following blue-light exposure; MSC-sEV and MSC-sIV treatment significantly attenuated this increase (Supplementary Fig. 12a,b). Compared with MSC-sEVs, MSC-sIVs showed a more pronounced inhibitory effect on GFAP protein (Supplementary Fig. 10). In mice not exposed to blue light, well-organized IBA1-positive cells were detected in the inner retinal layer, while fewer IBA1-positive cells were in the outer retinal layer (Supplementary Fig. 12c). In contrast, many irregularly arranged IBA1-positive cells were in the whole retinas of mice subjected to blue-light exposure, indicating microglial activation. In the MSC-sEV and MSC-sIV treatment groups, microglial activation was suppressed. The same dosage of MSC-sIVs exerted a more substantial inhibitory effect on microglial activation than MSC-sEV treatment (Supplementary Fig. 12d–f). Therefore, MSC-sIVs exhibited a superior capacity to inhibit retina-reactive gliosis in light-induced retinal damage compared with MSC-sEVs.

MSC-sIVs better restore retinal structure and function of rd10 mice than MSC-sEVs

Next, we determined whether MSC-sIVs can restore retinal degeneration in rd10 mice, a model characterized by photoreceptor degeneration due to a mutated *Pde6b*. We initially utilized H&E staining to observe the structure of the retina on postnatal day (p) 28. Consistent with previous findings[38], rd10 mice at p28 exhibited an obvious loss of cells in the ONL (Fig. 5a), whereas MSC-sEV and MSC-sIV treatments reversed these alterations, with MSC-sIVs demonstrating a notably superior effect to MSC-sEVs (Fig. 5b). At p28, the ERG waveforms of rd10 mice were extinguished, representing a collapse of photoreceptor cell function (Fig. 5c). However, MSC-sEV and MSC-sIV treatment notably rescued the light responses of rd10 retinas (Fig. 5d). MSC-sEVs significantly improved the *a*- and *b*-wave amplitudes at medium–high stimulation (>1.0 cd.s m^{-2}), whereas MSC-sIVs enhanced both amplitudes under all stimulations (>0.1 cd.s m^{-2}). Furthermore, MSC-sIV therapy restored *a*-wave (at the highest stimulation) and *b*-wave (at medium–high stimulation) amplitudes more effectively than MSC-sEV therapy (Fig. 5d). Hence, MSC-sIVs were better than MSC-sEVs in ameliorating retinal damage and improving visual function in rd10 mice.

The loss of photoreceptor cells in the retina diminished rhodopsin expression (Fig. 5e), whereas both MSC-sEV and MSC-sIV treatments preserved rhodopsin levels, with MSC-sIVs demonstrating a notably superior effect (Fig. 5f). To determine the effects of MSC-sIVs on retinal synaptic connections in rd10 mice, PSD95 (a postsynaptic-associated protein presenting within the presynaptic terminals of photoreceptor neurons) was stained in the retinas. PSD95 expression was considerably weak in rd10 retinas (Fig. 5g), whereas MSC-sEV and MSC-sIV treatments rescued this decline, with the restorative efficacy of MSC-sIVs being markedly better than that of MSC-sEVs (Fig. 5h).

At p28, retinal sections from euthanized rd10 mice were stained with TUNEL and DAPI. The apoptotic signals were primarily concentrated in the ONL of the retina (Fig. 5i). In contrast, rd10 mice treated with MSC-sEVs and MSC-sIVs displayed reduced apoptotic signals, with apoptosis being more suppressed in the MSC-sIV than in the MSC-sEV treatment group (Fig. 5j). Bax activation has been reported to occur consistently across three retinitis pigmentosa models, exhibiting both upregulated total protein levels and intensified localization within photoreceptors[39,40]. In our investigation, apoptosis-related proteins were markedly increased in the retinas of rd10 mice (Supplementary Fig. 13a). At equivalent doses, MSC-sIVs reduced caspase3 activation, decreased the expression of Bax and upregulated BCL-2 (Supplementary Fig. 13b–f), whereas MSC-sEVs had no effect. Thus, the anti-apoptosis effect of MSC-sIVs is superior to that of MSC-sEVs in treating retinal degeneration in rd10 mice.

Next, we performed immunostaining to evaluate the expression of GFAP and IBA1 in rd10 retinas. Similar to the mice suffering from light-induced retinal damage, the rd10 retina exhibited Müller cell activation (Supplementary Fig. 14a); while MSC-sEV and MSC-sIV treatments decreased GFAP expression, sIVs demonstrated significantly superior effects (Supplementary Fig. 14b). In rd10 mice, an increased number of disorganized IBA1-positive cells were observed across all retinal layers, particularly in the outer retina, where microglial cells displayed reactive morphologies (characterized by enlarged cell bodies and retracted processes) (Supplementary Fig. 14c). While both MSC-sEVs and MSC-sIVs significantly decreased retinal IBA1-positive cells, MSC-sIVs achieved a more pronounced reduction (Supplementary Fig. 14d). Western blotting further supported the changes in GFAP, PSD95 and rhodopsin levels in the rd10 mouse retina (Supplementary Fig. 15). Therefore, as noted in light-induced retinal damage, intravitreal injection of MSC-sIVs has a better anti-gliosis effect than MSC-sEVs in retinal degeneration in rd10 mice.

Fig. 4 | Therapeutic effects of MSC-sIVs and MSC-sEVs on blue-light-damaged mice (BL). a, Representative topographic map of the retinal thickness. L, low-dose vesicles (2 μg); H, high-dose vesicles (4 μg). **b**, Representative spectral domain-OCT scans of the retina. White lines demarcate the region of interest for retinal thickness analysis. **c**, Retina thickness measurement. Six eyes, one from each mouse, were analysed ($n = 6$). **d**, Representative retinal images following H&E staining in each group (GCL, ganglion cell layer; INL, inner nuclear layer; ONL, outer nuclear layer). The number of nuclei within the ONL layer was quantified within the area delineated by the white dashed lines. **e**, The number of nuclei in the ONL extends outward along the dorsal/superior (positive values on the abscissa) and ventral periphery/inferior (negative numbers on the abscissa) directions, beginning at 250 μm from the optic nerve head and continuing every 250 or 500 μm. Four eyes, one from each mouse, were analysed ($n = 4$). '@' indicates significant differences between BL-sIVs-H and BL-PBS, '#' indicates significant differences between BL-sEVs-H and BL-PBS. Other statistical data are available in the source data. **f**, Representative ERG waveforms recorded in response to a stimulus flash (2.2 log(cd.s m^{-2})) from a single eye of a mouse in each treatment group. **g**, Average amplitudes of ERG *a*- and *b*-waves from each treatment group. Eight eyes, one from each mouse, were analysed ($n = 8$). The statistical differences between groups at a stimulation intensity of 2.2 were as follows: A < 0.0001, B = 0.0063, C = 0.2656, D = 0.0084, E = 0.0010, F = 0.4388, G = < 0.0001, H < 0.0001, I < 0.0001, J < 0.0001, K < 0.0001, L = 0.3081. Other statistical data are available in the source data. **h**, Immunofluorescence analysis of rhodopsin (green) expression in retinas. Blue, DAPI. **i**, Relative expression of rhodopsin in retinas. Four eyes, one from each mouse, were analysed ($n = 4$). **j**, Representative morphological images of retina sections. Green, TUNEL staining; blue, DAPI. White dashed lines indicate the area used for quantitative analysis. **k**, Ratio of TUNEL-positive nuclei in photoreceptors. Four eyes, one from each mouse, were analysed ($n = 4$). The data in **c**, **e**, **g**, **i** and **k** are expressed as mean ± s.e.m. and analysed using one-way ANOVA.

https://doi.org/10.1038/s41551-025-01596-1

MSC-sIVs ameliorate retinal injury by inhibiting ER stress

To elucidate the therapeutic mechanism of MSC-sIVs in treating light-induced retina injury in normal mice and retinal degeneration in rd10 mice, retinas were collected from mice treated with MSC-sIVs or PBS at 7 days post therapy. RNA-seq analysis revealed the top 15 differentially enriched pathways between PBS- and MSC-sIV-treated groups (Fig. 6a,b). One carbon pool by folate and calcium ion signalling ranked in the top two responsive pathways in light-induced retina injury (Fig. 6a), whereas recycling of L1, L1CAM interaction, IRE1alpha activation of chaperone proteins, XBP1(S) activation of chaperone

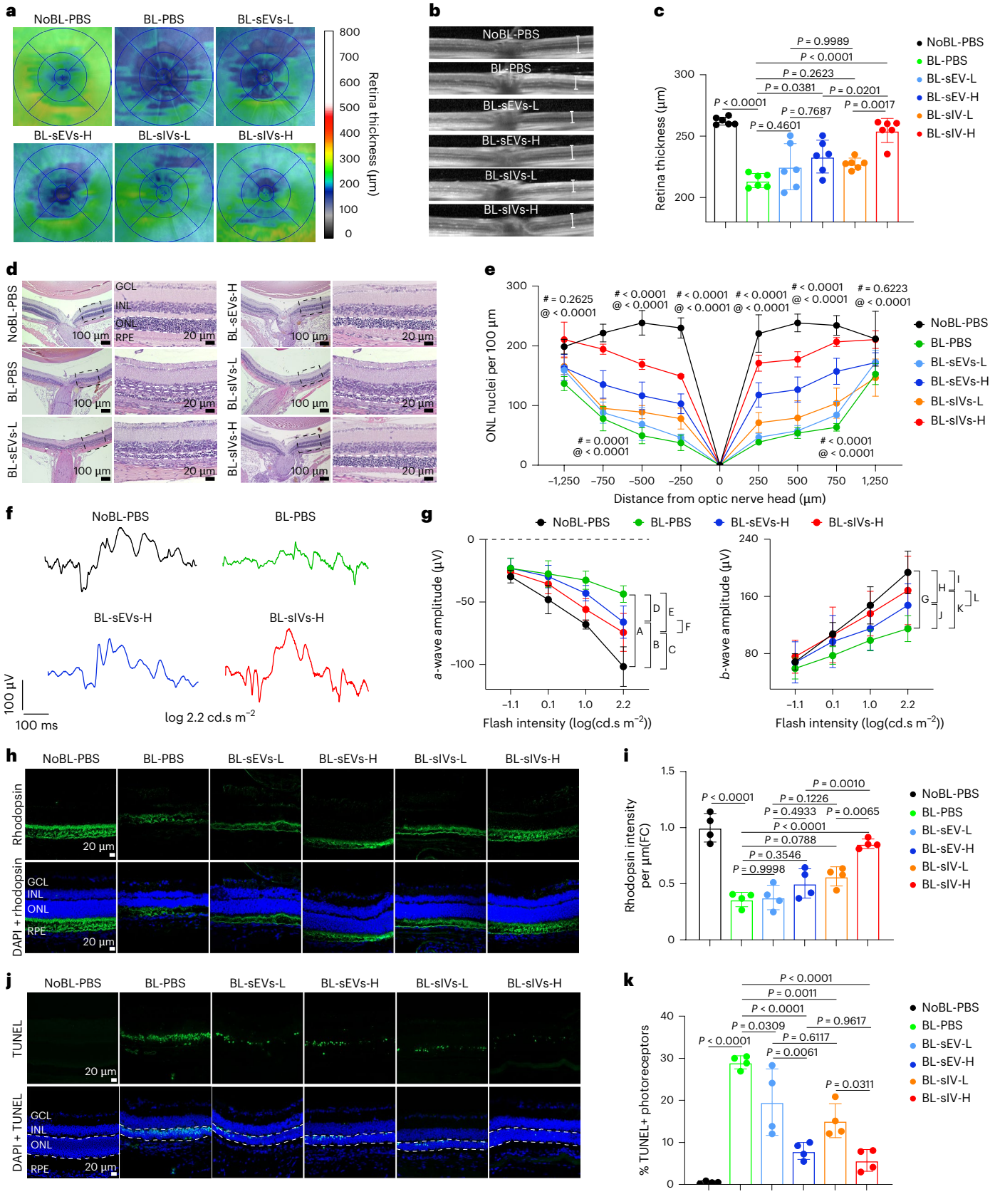

https://doi.org/10.1038/s41551-025-01596-1

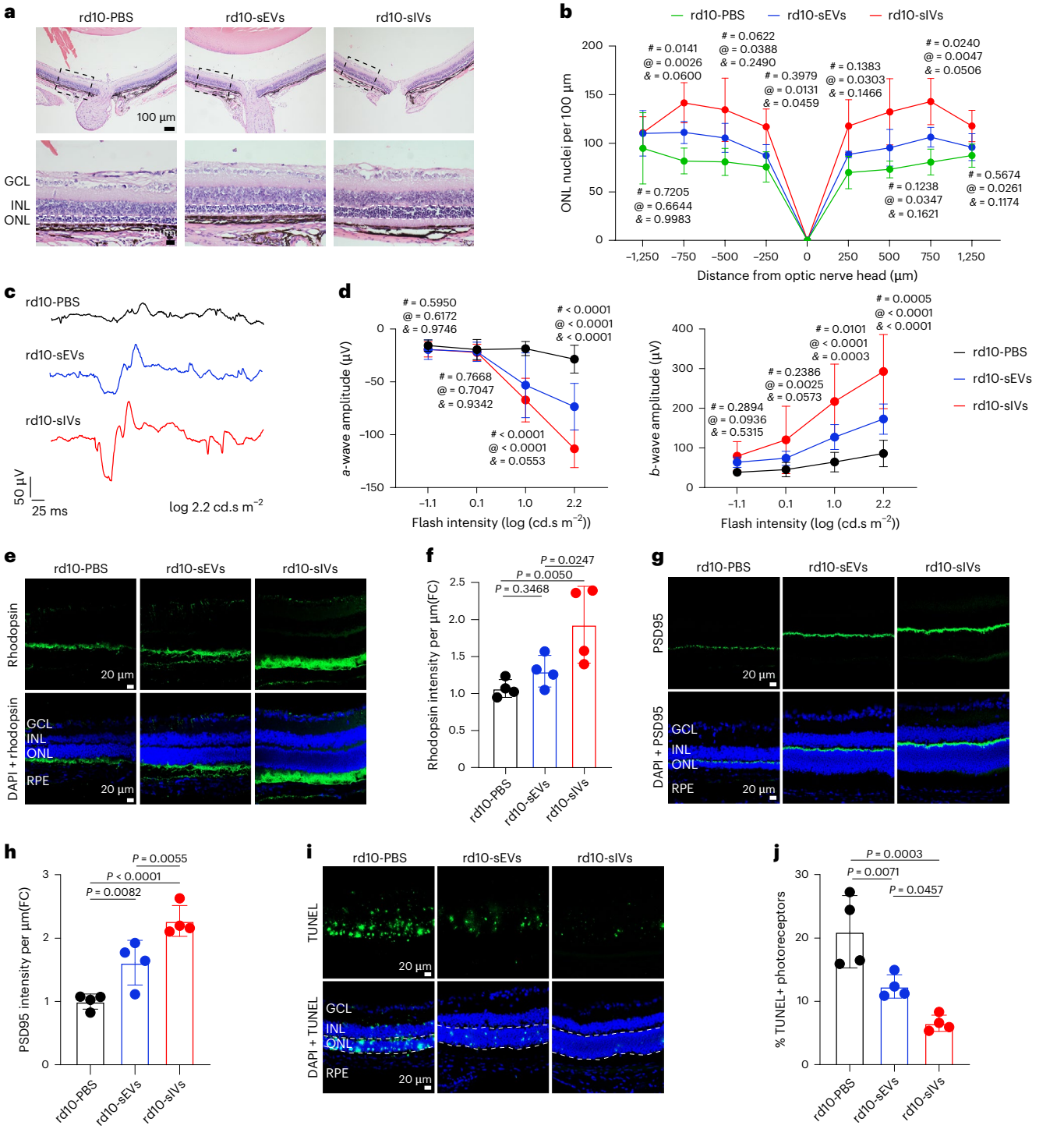

Fig. 5 | Therapeutic effect of MSC-sIVs and MSC-sEVs in rd10 mice. **a**, Representative retinal images were taken after H&E staining in each group. The nuclei within the ONL were quantified within the area delineated by the white dashed lines. **b**, Number of nuclei in ONL of 8 discrete regions of retinal sections starting at 250 μm from the optic nerve head and extending every 250 or 500 μm outward along the dorsal/superior (positive values on the abscissa) and ventral periphery/inferior (negative numbers on the abscissa) directions. Five eyes, one from each mouse, were analysed ($n = 5$). '@' indicates significant differences between rd10-sIVs and rd10-PBS, '#' indicates significant differences between rd10-sEVs and rd10-PBS, '&' indicates significant differences between rd10-sEVs and rd10-sIVs. **c**, Representative electroretinogram recordings from one eye in each treatment group under stimulus flash (2.2 log(cd.s m^{-2})). **d**, Average amplitudes of ERG *a*- and *b*-waves from each treatment group. Nine eyes, one from each mouse, were analysed ($n = 9$). '@' indicates significant differences between rd10-sIVs and rd10-PBS, '#' indicates significant differences between rd10-sEVs and rd10-PBS, '&' indicates significant differences between rd10-sEs and rd10-sIVs. **e**, Immunofluorescence of rhodopsin (green) expression in retinas. Blue, DAPI. **f**, Relative expression of rhodopsin in retinas. Four eyes, one from each mouse, were analysed ($n = 4$). **g**, Immunofluorescence of PSD95 (green) expression in retinas. Blue, DAPI. **h**, Relative expression of PSD95 in retinas. Four eyes, one from each mouse, were analysed ($n = 4$). **i**, Representative morphological images of retina sections. Green, TUNEL staining; blue, DAPI. White dashed lines indicate the area used for quantitative analysis. **j**, Ratio of TUNEL-positive nuclei in photoreceptors. Four eyes, one from each mouse, were analysed ($n = 4$). The data in **b**, **d**, **f**, **h** and **j** are expressed as mean ± s.e.m. and analysed using one-way ANOVA.

https://doi.org/10.1038/s41551-025-01596-1

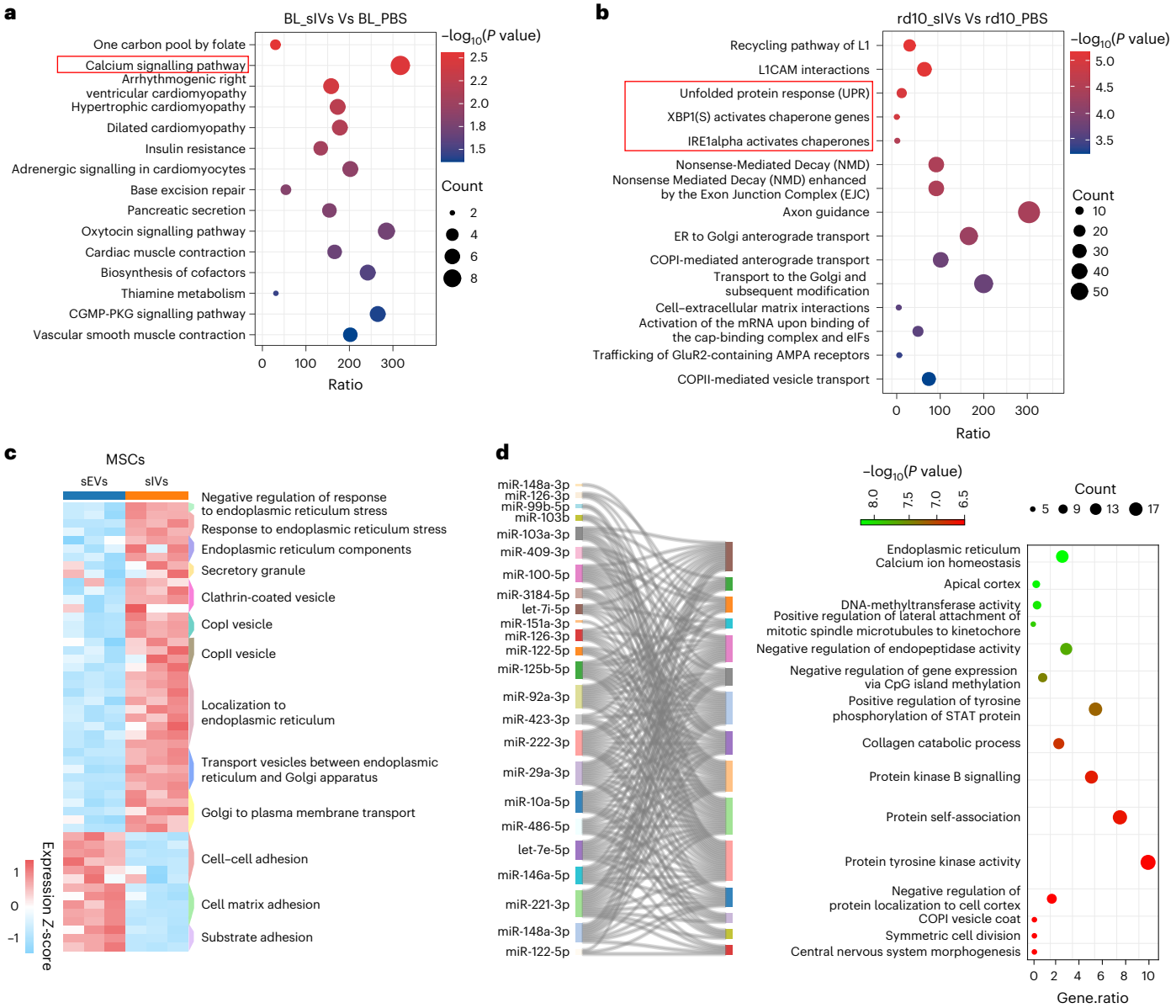

Fig. 6 | Inhibitory role of MSC-sIVs on ER stress in the retinas of light-damaged and rd10 mice. a, RNA sequencing of the retinas revealed pathway alterations between BL-PBS and BL-sIVs groups. **b**, RNA sequencing of the retinas revealed pathway alterations between rd10-PBS and rd10-sIVs groups. **c**, Heat map showing the score of typical intracellular pathways of total proteins in MSC-sIVs and MSC-sEV analysed using gene set variation analysis. **d**, Pathway enrichment analysis of target genes for differential miRNAs in the top 50 high-abundance miRNAs from MSC-sIVs and MSC-sEVs. **e**, Western blot analysis of ER stress-related proteins in the retinas of light-damaged mice. **f**,**g**, Western blot analysis of ER stress-related proteins in the retinas of rd10 mice at p21 (**f**) and p28 (**g**). Data in **a**–**d** were analysed using two-tailed unpaired Student's *t*-test. Representative images are shown in **e**–**g**; similar results were obtained in at least 3 independent experiments.

protein genes, unfolded protein response (UPR), activation of mRNA upon eIFs and cap-binding complex binding ranked in the top five responsive pathways in the rd10 model (Fig. 6b). Thus, MSC-sIVs exert therapeutic effects through cellular metabolism and ER stress responses.

To investigate the role of the proteins in treating retinal injury, pathway enrichment analysis of total proteins in the two types of vesicle was performed via gene set variation analysis. Negative regulation of the ER stress response was enriched in MSC-sIVs, whereas cell-to-cell adhesion and cell-to-matrix adhesion were enriched in MSC-sEVs (Fig. 6c). Subsequently, we extracted the top 50 miRNAs expressed in sEVs and sIVs derived from MSCs (Supplementary Fig. 16) and selected 24 significantly different miRNAs for target gene enrichment analysis. The ER calcium ion homeostasis pathway was identified as a top pathway co-regulated by these miRNAs (Fig. 6d).

Prolonged ER stress leads to cell apoptosis and retinal structure and function damage[41]. Blue-light exposure led to a significant elevation of ER stress-related proteins, including GRP78, p-PERK/PERK, IRE1α, ATF6, p-eIF2α and CHOP, in the retina (Fig. 6e and Supplementary Fig. 17). MSC-sIVs at low or high doses partially reduced the expression levels of these ER stress-related proteins, whereas MSC-sEVs had no such effects (Fig. 6e and Supplementary Fig. 17). Moreover, rd10 mouse retinas showed a partial increase in ER stress-related proteins (GRP78, IRE1α, ATF6 and CHOP) at 7 days (Fig. 6f and Supplementary Fig. 18), whereas at 14 days, the expression of GRP78, p-PERK/PERK, PERK, IRE1α, ATF6, p-eIF2α/eIF2α and CHOP was markedly elevated (Fig. 6g and Supplementary Fig. 19). MSC-sIVs decreased the levels of ER stress-related proteins in rd10 mice at 7 and 14 days, whereas MSC-sEVs elicited marginal effects (Fig. 6f,g). MSC-sIVs suppressed ER stress in the retinas of light-damaged mice and rd10 mice, partially contributing to their prominent therapeutic effect in these animal models.

MSC-sIVs are richer in neuroprotective factors than MSC-sEVs

MSCs synthesize and secrete abundant inflammation regulatory and neuroprotective factors, which exert neuroprotective effects[42]. Therefore, we compared the levels of cytokines carried by MSC-sIVs and MSC-sEVs. Proteomic analysis revealed that MSC-sIVs contained lower levels of interleukin (IL)-1β and insulin-like growth factor 2 (IGF2) than MSC-sEVs (Supplementary Fig. 20a). Subsequently, an enzyme-linked immunosorbent assay revealed that, on an equal mass basis, MSC-sIVs contained elevated levels of neuroprotective and anti-inflammatory factors, including basic fibroblast growth factor (bFGF), IGF-1, epidermal growth factor (EGF) and IL-10 (Supplementary Fig. 20b). Meanwhile, MSC-sIVs showed decreased TNF, whereas IL-6 levels remained similar between the two vesicle groups (Supplementary Fig. 20b). Hence, MSC-sIVs have a stronger neuroprotective potential than MSC-sEVs, contributing to their significant therapeutic effect in retinal injury animal models.

MSC-sIVs exhibit higher cellular and tissue uptake, enhanced drug-loading capacity and improved therapeutic efficacy compared with MSC-sEVs

Cell-derived vesicles have a stable structure, which allows them to be directly absorbed by tissues or serve as an effective drug carrier for drug delivery. We evaluated the tissue uptake and drug-loading capabilities of sIVs. MSC-sIVs exhibited enhanced internalization in retinal pigment epithelial (RPE) cell and human retinal microvascular endothelial cell (HRMEC) co-cultures during 12–48 h of observation (Extended Data Figs. 4a–d and 5). Subconjunctival injection demonstrated deeper penetration of MSC-sIVs into the retina than of MSC-sEVs (Extended Data Fig. 4e,g). Intravitreally injected MSC-sIVs diffused rapidly across retinal layers by 8 h, achieving enhanced distribution throughout the entire retina by 24 h, whereas MSC-sEVs were limited (Extended Data Fig. 4f,h). Hence, the enhanced retinal uptake of sIVs may partially explain their superior protective effects in retinal damage compared with sEVs.

Next, we investigate the drug delivery capacity of MSC-sEVs and MSC-sIVs by encapsulating the lipophilic small molecule Rapa using ultrasonication. Rapa has been shown to exhibit notable pharmacological effects, including anti-oxidative, anti-inflammatory and anti-apoptotic properties, and has shown therapeutic potential in animal models of retinal damage[43,44]. However, intravitreal injection of hydrophobic Rapa may lead to crystallization in the vitreous, requiring the use of a delivery carrier to enhance its efficacy[45]. We employed ultrasound-assisted loading to encapsulate Rapa into vesicles. Both MSC-sEVs and MSC-sIVs maintained their structural integrity and vesicle size without noticeable alterations post loading (Supplementary Fig. 21a,b). High-performance liquid chromatography (HPLC) analysis showed that MSC-sIVs exhibited much higher encapsulation and loading efficiencies compared with MSC-sEVs (Fig. 7b,c). Subsequently, in vitro drug release was assessed using the dialysis bag method. Pure Rapa exhibited minimal cumulative release, whereas vesicle encapsulation enhanced both drug stability and release kinetics (Supplementary Fig. 22). Specifically, sIVs demonstrated superior cumulative release performance compared with sEVs during the 7-day observation period (Supplementary Fig. 22). For in vivo delivery, both vesicles carrying equal amounts of Rapa, along with the same amount of pure Rapa, were individually injected into the subconjunctival space and mouse vitreous cavity. HPLC analysis showed that at 24 h post subconjunctival injection, the retina absorbed a considerably higher amount of Rapa from vesicles than following direct Rapa injection, whereas from 48 h to 5 days, the retina absorbed more Rapa from MSC-sIVs than from MSC-sEVs (Fig. 7d). After intravitreal injection, more Rapa was detected in the retina in the MSC-sIV group than in the MSC-sEV and pure Rapa groups at 24 h (Fig. 7e).

Having established that MSC-sIVs deliver more Rapa in vivo, we next evaluated their therapeutic efficacy by administering equal doses of Rapa encapsulated in MSC-sIVs and MSC-sEVs in the

Fig. 7 | Comparison of drug-loading capacities and therapeutic efficacy of rapamycin (Rapa)-loaded sEVs and sIVs in blue-light-damaged mice. **a**, Experimental workflow: (1) Rapa was encapsulated into vesicles using ultrasonication, with subsequent quantification of loading efficiency by HPLC analysis. (2) The in vivo drug delivery efficacy of Rapa-loaded vesicles (containing equivalent amounts of Rapa) was evaluated following subconjunctival and intravitreal administration, with pure Rapa serving as the control. Retinal Rapa concentrations were quantified by HPLC. (3) The therapeutic effects of Rapa-loaded vesicles (containing equivalent Rapa amounts) on a light-induced retinal damage model were evaluated, with drug-free vesicles and pure Rapa serving as controls. **b**, Encapsulation efficiency of sEVs and sIVs for Rapa ($n = 6$ biologically independent samples). **c**, Drug-loading efficiency of sEVs and sIVs for Rapa ($n = 6$ biologically independent samples). **d**, Retinal Rapa content following subconjunctival injection ($n = 5$ biologically independent samples for 24 h, $n = 4$ biologically independent samples for 48 h and 5 days). **e**, Retinal Rapa content following intravitreal injection. Five eyes, one from each mouse, were analysed ($n = 5$). **f**, Representative H&E-stained retinal images for each group. Nuclei within the ONL were quantified in the area demarcated by white dashed lines. **g**, Average amplitudes of ERG *a*- and *b*-waves from each treatment group. Six eyes, one from each mouse, were analysed ($n = 6$). Significant differences between BL-PBS and all other groups are indicated in the figure. Other statistical data are available in the source data. **h**, Representative retinal section images from each group. Green, TUNEL staining; blue, DAPI. **i**, Ratio of TUNEL-positive nuclei in retinal photoreceptors. Five eyes, one from each mouse, were analysed ($n = 5$). **j**, Western blot analysis revealed alterations in the mTOR signalling pathway. Data shown are representative of 3 independent replicates yielding comparable results. **k**, Relative expression levels of p-mTOR ($n = 4$ biologically independent samples for the NoBL-PBS and BL-sIV-Rapa groups; $n = 5$ biologically independent samples for other groups). Data in **b**–**e**, **g**, **i** and **k** are presented as mean ± s.e.m. and were compared using two-tailed unpaired Student's *t*-test (**b**,**c**), two-way ANOVA (**d**,**g**) and one-way ANOVA (**e**,**i**,**k**). Schematic in **a** was drawn using pictures from Biovisart (https://biovisart.com.cn).

https://doi.org/10.1038/s41551-025-01596-1

blue-light-induced retinal injury model. Studies have reported that Rapa protects photoreceptor cells from apoptosis by inhibiting the mTOR signalling pathway[46,47]. Consistently, we observed mTOR pathway activation in the retina at 48 h after blue-light exposure (Supplementary Fig. 23). To compensate for the lower drug-loading capacity of sEVs compared with sIVs, we adjusted the doses of vesicles (1.7 μg sEVs vs 0.8 μg sIVs) to ensure equivalent Rapa delivery, using equal amounts of empty vesicles as negative controls. Quantitative analysis confirmed that all Rapa-loaded vesicle formulations effectively mitigated retinal thinning and photoreceptor

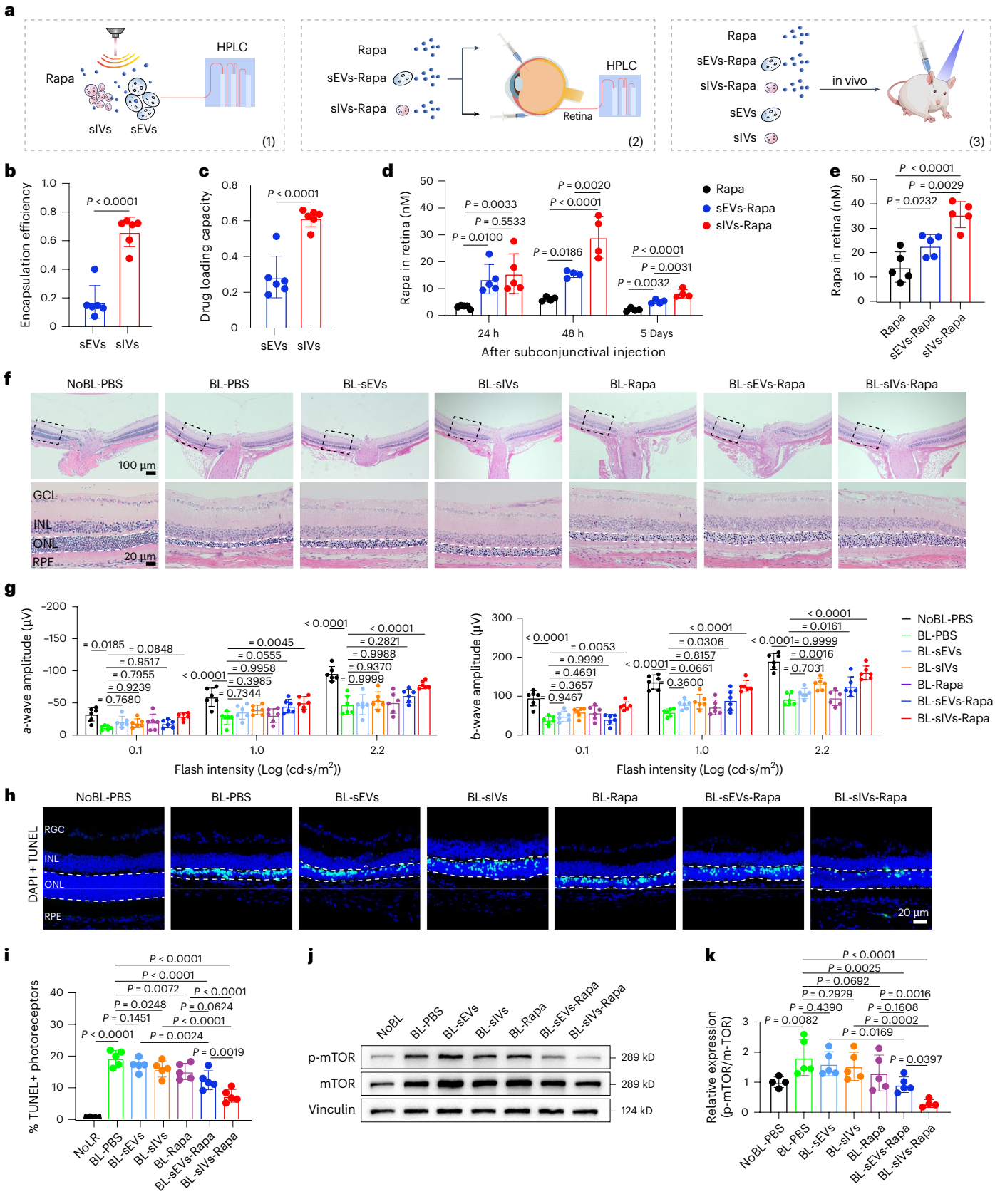

cell loss, restored retinal electrophysiological function and reduced apoptosis (Fig. 7f–i, and Supplementary Figs. 24 and 25). Among these, sIV-Rapa exhibited superior therapeutic efficacy over sEV-Rapa. In contrast, both free Rapa and unloaded vesicles showed negligible therapeutic effects, attributable to the solubility limitations of Rapa and subtherapeutic vesicle concentrations (much lower than the doses used in the above experiments). Western blotting analysis revealed that both unloaded vesicles and free Rapa had little effect on mTOR signalling, while both sIV-Rapa and sEV-Rapa demonstrated a pronounced suppression of mTOR pathway activation, with sIV-Rapa showing greater inhibition (Fig. 7j,k). These results conclusively establish the advantages of sIVs as nanoscale drug carriers through enhanced therapeutic delivery efficacy.

Discussion

Although the characteristics and therapeutic applications of EVs, especially exosomes, have been widely explored, there are currently no available reports on the isolation, enrichment, omics analysis or application exploration of intracellular vesicles. Here we report the characterization of a group of small nanovesicles isolated from cells, termed sIVs. sIVs are defined as endogenous nanovesicles (30–100 nm in diameter) intrinsically present in cells, possessing native bilayer lipid membranes and characterized by TMEM214 protein expression. Their intracellular origin and nanoscale architecture confer a lipid-rich composition, providing enhanced biocompatibility and superior loading capacity for hydrophobic therapeutic agents. These intrinsic properties establish sIVs as promising candidates for clinical translation.

Various engineering approaches, such as extrusion and osmotic lysis, can disrupt cell membranes and reassemble them into engineered vesicles[7,48]. It has been recently reported that vesicles similar in size to sEVs were obtained from dental pulp stem cells through repeated freeze–thaw cycles and identified as premature exosomes[9]. In this study, we isolated and identified vesicles inherently present within cells, termed sIVs, which are distinct from sEVs and exhibit low expression of major exosome markers. Instead, sIVs are enriched in proteins associated with membrane-bound organelles, the clathrin protein family and intracellular transport vesicles, suggesting a role in organelle communication and coated vesicle transport[49]. TMEM214 was identified as a specific marker for sIVs, with TMEM214-positive nanovesicles directly visualized inside cells, confirming their endogenous origin. Cells contain various types of IV, including secretory vesicles, COP-coated transport vesicles, clathrin-coated vesicles and transport vesicles facilitating ER–Golgi trafficking. Given their intracellular origin, the sIVs isolated in this study probably represent a heterogeneous population comprising multiple vesicle subtypes involved in distinct cellular transport processes. The formation of IVs involves the budding of intracellular membrane compartments, including the ER, Golgi apparatus and endosomes[15]. Unlike sEV secretion, which is tightly regulated and comparatively slower[50], intracellular organelle communication via IVs is a continuous process, potentially explaining the higher abundance of sIVs in cells.

miRNAs with specific biological roles are the most widely studied class of sRNAs in sEVs. In our study, miRNAs were the most abundant sRNA species in sIVs, accounting for over 90% of MSC-sIVs, suggesting that sIVs have multiple biological regulatory potentials. YRNAs were the most abundant sRNA species in sEVs, consistent with previous literature[51,52]. The differential miRNA target genes between sIVs and sEVs are associated with intracellular membrane-bound organelles, providing evidence for miRNA transport by sIVs inside the cells. Our results also showed that differential miRNA target genes between MSC-sIVs and MSC-sEVs are associated with pathways involved in neural development and immune regulation, which are closely related to the regulatory functions of MSCs[42,53–56], suggesting that miRNAs in sIVs exhibit merocyte characteristics.

Lipidomic analyses revealed that sIVs contained higher amounts of PC and PE than sEVs. IVs are closely associated with the ER and Golgi apparatus, and glycerophospholipids are predominantly synthesized within the ER, which explains the high levels of glycerophospholipids in sIVs. Membrane bending and lipid distribution play crucial roles in intracellular transport[57–59], and glycerophospholipids, along with cholesterol, regulate membrane curvature and fluidity, facilitating the dynamic fusion and fission of sIVs[60,61]. Notably, MSC-sIVs were rich in phosphatidylcholine (lecithin), which has been shown to enhance drug delivery efficiency[62,63] and protect vesicles from lysosomal degradation[64]. The intracellular uptake and transport efficiency of nanoscale particles correlate with size[65–67], as nanoparticles within 50-nm diameter have the greatest impact on the basic functions of target cells[68], and exomeres (<50 nm) exhibit enhanced liver uptake following systemic injection[69]. Given that sIVs are much smaller than sEVs, their lipid characteristics and small size may facilitate improved tissue uptake, enhanced biological barrier penetration and superior drug delivery efficiency.

MSC-sIVs demonstrated superior therapeutic efficacy over MSC-sEVs in two retinal injury models: the blue-light-induced damage model and rd10 mice. Notably, ER stress plays a pivotal role in the pathogenesis of retinal injury[41,70–72], and alleviating ER stress can effectively relieve retinal degeneration[31,73,74]. Our RNA-seq results indicated that MSC-sIV treatment influenced calcium signalling and the cGMP-PKG pathway in the light-damage model, and regulated ER stress signalling in rd10 mice. Since the ER is a major calcium reservoir, dysregulated calcium homeostasis is known to exacerbate ER stress, triggering the UPR and amplifying damage. Blue-light exposure increases retinal cGMP levels, rapidly activating the PERK pathway of the UPR, which directly induces ER stress and worsens injury[75]. Our proteomic analyses further supported the involvement of MSC-sIVs in ER transport and cellular responses to ER stress, with a pronounced capacity to negatively regulate ER stress-related pathways. In addition, target gene enrichment analysis indicated that high-abundance miRNAs in MSC-sIVs help maintain ER calcium homeostasis. Importantly, western blotting analysis confirmed that MSC-sIVs significantly reduced ER stress-related proteins in both models, whereas MSC-sEVs had minimal effect. Collectively, MSC-sIVs protect retinas from degeneration, at least in part, by inhibiting ER stress.

Notably, exosomes exhibit intrinsic homing properties, as demonstrated by endothelial cell-derived exosomes that selectively traffic to vascular endothelia through the bloodstream[76]. Given their intracellular origin, sIVs may have distinct organelle-targeting capabilities, which could provide a key advantage in drug delivery applications. In contrast to sEVs, which must undergo endocytosis and endosomal escape to reach intracellular targets, sIVs may directly interact with subcellular structures. Our proteomic profiling combined with BFA blockade experiments indicates that sIVs are involved in ER-to-Golgi transport, which may explain their ability to modulate ER stress pathways in retinal cells. In addition, sIVs demonstrate superior therapeutic efficacy in drug delivery compared with sEVs, probably due to their intracellular targeting capability. This observation highlights the possibility of designing sIVs to target specific organelles.

As a major type of IV, secretory vesicles mediate protein secretion[77]. MSCs secrete various neurotropic factors with neuroprotective effects[78,79]. Our results showed that MSC-sIVs contained more neuroprotective factors and fewer inflammatory factors than MSC-sEVs, which might be related to the protein components of secretory vesicles among sIVs. To maximize therapeutic precision across a wider range of fields, future studies could engineer nanoparticle systems combining key beneficial factors identified in MSC-sIVs. For instance, neuroprotective factors within sIVs can be overexpressed through genetic engineering, or ultrasound-mediated drug delivery systems can be employed to load anti-tumour agents for precise therapy. Moreover, the membrane of sIVs can be designed to possess targeting

properties, leveraging their small size and stability, which may hold substantial potential for tumour therapy.

Currently, besides sEVs and sIVs, many other nanovesicles, such as liposomes, artificial cell-derived vesicles and plant-derived exosome-like nanoparticles, are being applied in biotherapy. As shown in Supplementary Table 2, compared to these vesicle-based systems, sIVs offer significant advantages in yield, stability and therapeutic potential. The isolation of sIVs is simpler, requiring less cellular processing and fewer centrifugation steps. Naturally occurring within cells, sIVs can be isolated in 20–40 times greater quantities than sEVs, enhancing scalability. They exhibit superior stability under physiological conditions compared with sEVs and temperature-sensitive liposomes. sIVs also have a small, uniform size (mainly 60–90 nm), improving cellular targeting and tissue distribution. These features make sIVs a promising platform for drug delivery and neuroprotection.

There are several limitations to this study that should be taken into account. The sIVs isolated herein represent a heterogeneous mixture of vesicle types. Although multiomic approaches were employed for characterization, precise methods to categorize these subpopulations remain underdeveloped. While low donor variability was observed in umbilical cord MSC-sIVs, individual discrepancies between different donors and even across different cell passages are inevitable. To address these challenges, future research should focus on refining isolation protocols to enhance reproducibility. Utilizing advanced technologies such as single-vesicle analysis and nano-flow cytometry will facilitate more in-depth molecular characterization[80] and aid in the identification of consistent patterns. Standardized protocols will minimize technical variability, while larger-scale studies with broader donor representation will strengthen the generalizability of findings. Moreover, while our findings indicate that MSC-sIVs can suppress ER stress, the precise molecular mechanisms underlying this effect have not been comprehensively elucidated. Future studies should aim to identify the key factors responsible for modulating ER stress, thereby advancing our understanding of the functional roles of sIVs.

In conclusion, sIVs represent a distinct class of intracellular nanovesicles with a molecular profile rich in organelle-associated proteins and miRNAs, a simple and efficient separation method and a high yield.

Their small size and cell-inherent properties enable efficient tissue uptake, enhanced biological barrier penetration and improved drug delivery, addressing key challenges in MSC-based therapies, such as uncontrolled proliferation of the cells and low sEV yields. These advantages position sIVs as a promising platform for regenerative medicine and targeted drug delivery.

Methods

Study approval

The mouse experiments were approved by the Tianjin Medical University Eye Institute Guidelines for Animal Research (No. TJYY2022122081).

Isolation and culture of MSCs

Human umbilical cords were sourced from Beijing Beilai Biotechnology and obtained from healthy volunteer donors without complications after caesarean sections. All participants or their guardians provided consent for the collection of samples and subsequent data handling. Identifiable information, including biological sex and age, is permitted for disclosure. Cells were cultured in DMEM/F12 medium (Invitrogen), and 10% fetal bovine serum (FBS, Invitrogen) and antibiotics (100 mg ml^{-1} streptomycin, 100 U ml^{-1} penicillin) were added as supplements. Proteomic, miRNA and lipidomic analyses utilized three biological replicates per group, derived from three independent donors.

Cell culture

The National Collection of Authenticated Cell Cultures provided the 293T and HeLa cell lines, which were examined to make sure mycoplasma contamination was absent. They were cultured in complete DMEM (Invitrogen) medium. The human RPE cell line APRE19 was obtained from the American Tissue Culture Collection (ATCC)[81]. APRE19 was maintained in DMEM/F12 (Invitrogen) supplemented with 10% FBS and antibiotics. Primary human retinal microvascular endothelial cells (HRMECs) (ACBRI 181) were acquired from Cell Systems and cultured following the procedures described in our previous publication[82]. Cells were cultured at 37 °C and 5% CO_2. Passages 3–8 were used for all experiments.

Mice

BALB/c mice (5–6 weeks, male, weighing 17 ± 1 g) were acquired from SPF. Professor Haiwei Xu of Southwest Medical University kindly donated the rd10 (Pde6brd10) mice (male, aged 2 weeks, weighing 5.5 ± 0.5 g) used. The C57BL/6J mice (male, aged 2 weeks, weighing 5.5 ± 0.5 g) were sourced from SPF. All experimental mice were male. The Department of Laboratory Animals maintained normal, pathogen-free housing for the animals, with a 12-h light/dark cycle and 4–5 mice per cage. Humidity was regulated at 41–44% to ensure animal welfare. The mice used in this investigation were fed a regular chow diet.

Collection of sIVs and sEVs

Upon reaching 90% confluency, cells were digested with trypsin, neutralized and rinsed three times with PBS. Cell density was adjusted to 1×10^6 cells per ml with PBS. During sonication, an ultrasound probe was positioned in the centre of the liquid surface while tubes were placed on ice. The cells were sonicated at 20% amplitude with a 15-s duty cycle, followed by 2 s on and 2 s off. After being sonicated, the liquid was moved to a fresh tube, centrifuged for 10 min at 2,000 × *g* and 30 min at 20,000 × *g*, and the supernatant passed through a 220-nm membrane. The supernatant was placed into an ultracentrifuge tube for further centrifugation at 150,000 × *g* for 70 min. All procedures were conducted on ice. The resulting pellet, representing small intracellular nanoparticles (sIVs), was resuspended in PBS. A step-by-step protocol is detailed in Supplementary Notes.

In summary, sEVs were isolated from cell culture medium using differential and gradient centrifugation[83]. The culture medium underwent stepwise centrifugation at 300 × *g*, 2,000 × *g* and 10,000 × *g* to clear cells and residual debris. This was followed by ultracentrifugation at 110,000 × *g* for 70 min, repeated twice, to pellet the extracellular vesicles. All the above centrifugation steps were performed at 4 °C.

Nanoparticle tracking analysis (NTA)

The vesicles were assessed using nanoparticle tracking with a NanoSight NS300 equipment (Malvern). Samples were diluted to a final volume of 1 ml with PBS and analysed at 25 °C. For each sample, three 60-s videos were captured. NTA results were examined using NTA software (NTA 3.3 Dev Build 3.3.104) in an automated manner. All measurements were repeated three times.

TEM

For sEVs and sIVs, following the pipetting of a 20-µl particle suspension (containing ~1 µg $µl^{-1}$) onto copper grids, the grids were covered and given 3 min to air-dry. The grids were then exposed to 20 µl of 1% phosphotungstic acid for 3 min. Subsequently, the samples were analysed using a transmission electron microscope (Hitachi HT7700).

Immunoelectron microscopy sample preparation

Vesicles and cells were incubated with anti-TMEM214 primary antibody, followed by colloidal gold-conjugated secondary antibody. After washing and fixation, vesicles were directly imaged by TEM. Cells were permeabilized, blocked with 5% BSA, post fixed, embedded in resin, polymerized at 60 °C, ultrathin sectioned (80 nm), mounted on copper grids and stained before TEM observation.

Western blot analysis

Cellular proteins were extracted using RIPA buffer and quantified with a bicinchoninic acid (BCA) assay (Solarbio). Samples were denatured, separated on SDS–PAGE gels and transferred onto PVDF membranes (Roche). Membranes were blocked and incubated with primary antibodies at 4 °C overnight, followed by HRP-conjugated secondary antibodies and detection via enhanced chemiluminescence (ECL). β-actin served as the loading control, and band intensities were measured using ImageJ (v.1.8.0_172).

Antibodies specific for the following proteins were used: Alix, HSP70, CD63, TSG10, TMEM214, GFAP, Caspase3, Rhodopsin, Bax, β-actin, BCL, PSD95, GRP78, IRE1, p-PERK, PERK, ATF, CHOP, cleaved-caspase3 and p-eIF2α, and eIF2α, EEA1, Rab7, mTOR, p-mTO and HRP-conjugated secondary antibodies.

Coomassie brilliant blue staining

The protein samples were separated by electrophoresis on a resolving gel following denaturation. Following separation, the gel was placed in a container containing Coomassie brilliant blue rapid staining solution (Beyotime) for 2 h. The gel that had been stained was subsequently extracted and subjected to multiple washes to achieve clear photographs.

Plasmid transfection and HIS-SIM imaging

The CD63-GFP plasmid and TMEM214-mCherry plasmid were procured from Gene Pharma. Plasmid transfection was performed according to manufacturer instructions. The acquisition and reconstruction of cell images were performed using a commercial structured illumination microscope (HIS-SIM)[84,85]. To enhance the clarity and distinction in reconstructed images, the technique of sparse deconvolution was employed[84,85].

BFA treatment

Cells were cultured to 50% confluence. BFA (MCE) was dissolved in dimethylsulfoxide to 25 mg ml^{-1} and further diluted in complete culture medium to 0 ng μl^{-1}, 25 ng μl^{-1} and 50 ng μl^{-1}. Subsequently, BFA stimulation was applied to the cells by exchanging the culture medium with medium containing BFA. After 24 h of stimulation, cell supernatant and cells were collected for further observation and analysis.

Mass spectrometric analysis

Proteins from cell lysates, sEVs and sIVs were quantified and trypsin digested, with peptide fractionation, library construction and proteomic data acquisition performed as previously described[86]. GO and pathway analyses were conducted using the Cytoscape plugin ClueGO. In pathway enrichment analysis, KEGG and Reactome databases were selected. The visualizations of heat maps, PCA scores, Venn diagrams and volcano plots were generated using the Hiplot software (https://Hiplot.com.cn) and the web platform (https://bioinformatics.com.cn). KEGG pathway analysis was performed using the Metascape online analysis software (http://metascape.org).

RNA isolation and library generation

Total RNA from sEVs and sIVs was extracted using the exoRNeasy Maxi kit (Qiagen) and assessed with a NanoDrop ND-1000 and Agilent 2100 Bioanalyzer. Target DNA fragments were recovered via PCR and used to construct cDNA libraries. Sequencing libraries were evaluated on an Agilent 2100 Bioanalyzer, clustered on a cBot system with the TruSeq SR Cluster Kit v3 (Illumina), and sequenced as 50-bp single-end reads on an Illumina HiSeq 2500/2000.

Untargeted metabolomic analysis

Untargeted lipid profiling of vesicles was conducted by Biotree Biotech. The metabolite extraction procedure was performed following the referenced protocol[87]. LC–MS/MS analysis was carried out using a UHPLC system (Thermo Fisher) equipped with a UPLC HSS T3 column (2.1 mm × 100 mm, 1.8 μm). The column was coupled to a Q Exactive HFX mass spectrometer (Thermo Fisher) for detection. MS/MS spectra were acquired on a QE mass spectrometer operating in data-dependent mode, managed via Xcalibur 4.0.27 (Thermo Fisher). In this mode, full-scan MS spectra were continuously analysed by the application.

Mouse model

For the blue-light-damage model, experiments were conducted in Balb/c mice following a 1-week acclimatization period (starting at 7 weeks of age) according to the referenced protocol[88]. After being in the dark for 16 h, the mice were exposed to intense blue light for 1 h. They were then put back in the dark for another 16 h. The mice were first subjected to pharmacological mydriasis to ensure full pupil dilation. Subsequently, they were placed in a chamber equipped with a blue-light source. About 2,000 lux of light were shone on each corner of the box. At 4 h before the 1-h light exposure, mice were given intravitreal doses of different amounts of MSC-sEV or MSC-sIV (2 μg or 4 μg in PBS solution) in a 1-μl volume. As a comparison, the same amount of PBS was used. The control group was made up of mice that were not exposed to light but were given 1 μl of PBS. Assessments and tissue collection were performed 5–7 days after model induction.

For rd10 mice, intravitreal injections were initiated at postnatal day 13 (p13). Littermates of rd10 mice received either MSC-sEVs (4 μg in 1 μl PBS), MSC-sIVs (4 μg in 1 μl PBS) or PBS (1 μl) at p13. Evaluations and euthanasia were performed at p21 and p28, followed by eyeball collection for further analysis.

Intravitreal injection

The mice were anaesthetized with sterile avertin (tribromoethanol, 300 mg kg^{-1}) by intraperitoneal injection. Mice received 0.5% tropicamide to induce full pupil dilation before the procedure. Then, 1 μl of MSC-sEVs, MSC-sIVs or PBS (negative control) was injected into the vitreous cavity without causing any lens damage. Injections were performed with a 34-gauge microsyringe (Hamilton). Each animal received an injection of the solution in only one eye.

OCT

Retinal structural changes were assessed using a Spectralis HRA + OCT system (Heidelberg Engineering) according to the referenced protocol[89]. One week after injection, a ring scan pattern (circular diameter 1, 3 and 6 ETDRS) centred on the optic nerve head was used to assess retinal thickness.

ERG

The ERG recording was made under scotopic (dark-adapted) condition[90–92]. The BABL/c (1 week after injection) and rd10 (2 weeks after injection) mice were subjected to an ERG evaluation in the dark after darkness adaptation (Phoenix Research). Intraperitoneal injections were administered to anaesthetize the mice, with reference electrodes positioned at the base of the tail and the forehead, while gold electrodes were affixed to the corneas. A light stimulus with a range of flash intensities (0.1, 1 and 2.2 log(cd.s m^{-2})) that lasted 1 ms was used to test the ERG. After every flash, recordings were made; amplitudes (μV) were recorded, and each measurement represents the average of three responses collected at interstimulus intervals of 1 s (0.1 log(cd.s m^{-2})), 10 s (1 log (cd.s m^{-2})) or 30 s (2.2 log(cd.s m^{-2})).

Histological assessment of mice retinas

BABL/c (1 week post injection) and rd10 (2 weeks post injection) mice were euthanized. After fixation in 4% paraformaldehyde, eyeballs were paraffin embedded and cut into 4-μm horizontal retinal sections, which were subsequently stained with H&E. Images of each section from a single eye were acquired with an inverted fluorescence microscope (Olympus).

Immunofluorescence and TUNEL staining for the retina

BABL/c (1 week post injection) and rd10 (2 weeks post injection) mice were euthanized. The staining procedures for the sections were conducted following manufacturer (Roche) instructions. Subsequently, retinal cryosections with a thickness of 6 µm were prepared, ensuring that the sections passed through the optic nerve whenever possible. Primary antibodies used in this study were: rhodopsin, GFAP, PSD95. To quantify TUNEL-positive signals, ImageJ software was used to measure the area of TUNEL-positive fluorescence and the corresponding area of nuclei within the ONL layer. For each group, five eyes were analysed. From each eye, three sections were obtained near the optic nerve, and five ×20-magnification images were captured from each section.

Quantification of RGCs and microglial cells

One week after blue-light-induced injury, mice were euthanized and eyeballs were collected. Retinal flat-mount staining was performed. Flat-mounted retinas were stained with RBPMS (Millipore, 1:200) or IBA1 (Abcam, 1:500) antibodies and incubated overnight at 4 °C in the dark for visualization of RGCs and microglial cells. A confocal fluorescence microscope (Carl Zeiss) was used to view retinas. RGCs and microglial cells were quantified using ImageJ (v.1.8.0_172)[32,33].

RNA sequencing and data analysis

RNA sequencing of the retina was conducted to investigate the differences in retinal gene expression following drug administration. For BALB/c mice, retinal samples were collected on the third day after blue-light exposure for RNA sequencing. For rd10 mice, RNA sequencing was conducted on day 7 following intravitreal injection. RNA-seq experiments were outsourced to Novogene.

Enzyme-linked immunosorbent assay

Twenty micrograms of both MSC-derived sEVs and sIVs were analysed using a kit, following the instructions provided by Cusabio and Abcam. The absorbance values of each well were quantified using a microplate reader.

Cellular uptake of DiD-labelled vesicles

Vesicles were incubated with lipophilic tracer DiD (Biotium) solution (5 µg ml^{-1}) at 37 °C for 30 min. Excess DiD was eliminated using an Amicon Ultra centrifugal filter (Merck, UFC5100). Cells were co-incubated with DiD-labelled vesicles (40 µg ml^{-1}) for 3, 12, 24 or 48 h. After washing and fixation, cells were stained with phalloidin (Proteintech) and DAPI (Solarbio). Finally, the cells were imaged via confocal laser scanning microscopy (LSM800, ZEISS). For flow cytometry, the negative control group is the group where DiD was co-incubated with PBS devoid of vesicles and washed following the same protocol as for vesicles. After digestion and washing, cells were first gated on FSC-A vs SSC-A to select live populations (Gate 1), and APC+ cells were subsequently identified via histogram analysis (Gate 2). Flow cytometric data were acquired on a FACSVerse instrument (BD Biosciences) and processed with FlowJo (v.10.8.1), following our earlier work[83]. All experiments were performed in triplicate.

Subconjunctival injection

For subconjunctival injection, after applying surface anaesthesia to the conjunctiva, we gently lifted the conjunctiva using toothless forceps and injected 6 µl of the solution beneath it through the temporal canthus using a 34G needle, ensuring coverage of approximately half the eyeball. Each animal received an injection of the solution in only one eye. To reduce the chance of infection, tobramycin ointment was administered to the ocular surface after the injection.

Retinal uptake of DiD-labelled vesicles

DiD-labelled vesicles were injected into the subconjunctiva of mice (6 µl, 4.8 µg). Eyeballs were collected for observation 24 and 48 h after the subconjunctival injection. Following subconjunctival injection, the red dye covered approximately half the volume of the posterior pole of the eye. In the tissue sections, a distinct red area was observed between the conjunctiva and choroid. To quantify the fluorescence intensity in the retina, we acquired consecutive ×20 images of this area and calculated the average fluorescence intensity, which served as the representative value for that retina. In addition, DiD-labelled vesicles were administered into the vitreous cavity of mice (1 µl, 0.8 µg). Eyeballs were collected for assessment at 8 h and 48 h following the vitreous injection.

Drug entrapment into sEVs and sIVs

A mixture of rapamycin (Rapa, Sigma-Aldrich) and sEVs or sIVs (9:1 ratio) was incubated for 10 min and then subjected to sonication. The sonication process involved applying a power level of 25% for six cycles; each cycle included a 30-s pulse followed by a 30-s rest. Subsequently, to enable recovery of the sEV membrane, the sample was held at 37 °C for 1 h. After sonication, free Rapa was eliminated using ultrafiltration centrifugation.

Rapa concentration determination using HPLC

Rapa concentration in Rapa-sEVs or Rapa-sIVs was assessed using HPLC (Thermo Scientific UltiMate 3000 series). The method for Rapa detection by HPLC was carried out following reported procedures[93]. Loading capacity (%) was calculated as the ratio of encapsulated drug to the combined mass of encapsulated drug and vesicles. Encapsulation efficiency (%) was defined as the proportion of the initial drug dose successfully entrapped within vesicles.

Retinal Rapa detection using LC–MS

Rapa stock solution (5 mM) was prepared in methanol and serially diluted to generate calibration standards (200–0.5 nM). Carbamazepine (2.00 mg ml^{-1}) in methanol served as the internal standard. Frozen retinal tissues were homogenized in 100 µl methanol; 50 µl homogenate was mixed with internal standard, vortexed, further extracted with 50 µl methanol and centrifuged (13,902 × g, 10 min). The resulting 100 µl supernatant was collected for HPLC analysis.

In vitro drug release

The in vitro drug release profiling was carried out according to a reported method with minor modification[94,95]. The formulation (1 ml) was enclosed in a dialysis bag with a 3.5-kDa molecular weight cut-off and suspended in 80 ml of PBS containing 0.5% Tween 80. The tubes were maintained at 37 °C with continuous shaking at 80 r.p.m. Every 8 h, 0.5 ml of supernatant was removed and an equal amount of fresh medium added to keep the total release medium constant. After suitable dilutions, the samples were analysed using a UV–Vis spectrophotometer (Hitachi) at 277 nm. A calibration curve was determined using the same medium. All measurements were performed in triplicate.

Statistical analysis and sample size determination

Statistical analyses were conducted in GraphPad Prism 8.0. To compare two groups, we employed the Student's t-test. For comparisons involving three or more groups, we applied one-way analysis of variance (ANOVA) followed by LSD post hoc tests. Two-way ANOVA assessed the influence of multiple factors and their interactions, with Tukey's post hoc test applied for pairwise comparisons. Statistically significant differences were defined as $P < 0.05$.

We performed a power analysis to ensure that the sample size was sufficient to detect biologically relevant effects with a statistical power of 80% and a significance level of 0.05:

$$n = \frac{2(\sigma^2)(Z_{\frac{\alpha}{2}} + Z_{\beta})^2}{2} \quad (1)$$

where $Z_{\alpha/2} = 0.96$ (for $\alpha = 0.05$) and $Z_{\beta} = 0.84$ (for 80% power) are the critical values for statistical significance and power, respectively. The expected effect size (Δ) and estimated standard deviation (σ) were derived from preliminary experiments and relevant literature.

Reporting summary

Further information on research design is available in the Nature Portfolio Reporting Summary linked to this article.

Data availability

The primary data underlying the findings of this study are included in the Article and its Supplementary Information. The mass spectrometry proteomics data have been deposited at the ProteomeXchange Consortium via the iProX partner repository with the dataset identifier PXD051827. The primary vesicle sequencing data from this study have been deposited in the Genome Sequence Archive (GSA-Human: HRA007464). All metabolic data are deposited in the MetaboLights platform (MTBLS12923). The RNA-sequencing data for rd10 mice and blue-light-damaged mice are available at the NCBI GEO under accession GSE309223 and GSE309258. Source data for the figures are provided in Supplementary Information and have also been deposited in figshare at https://doi.org/10.6084/m9.figshare.30226015 (ref. 96). Details of all commercially obtained reagents are provided in the Supplementary Key Resources Table. Source data are provided with this paper.

References

1. Kalluri, R. & LeBleu, V. S. The biology, function, and biomedical applications of exosomes. *Science* **367**, eaau6977 (2020).
2. Yáñez-Mó, M. et al. Biological properties of extracellular vesicles and their physiological functions. *J. Extracell. Vesicles* **4**, 27066 (2015).
3. Tkach, M. & Théry, C. Communication by extracellular vesicles: where we are and where we need to go. *Cell* **164**, 1226–1232 (2016).
4. Valadi, H. et al. Exosome-mediated transfer of mRNAs and microRNAs is a novel mechanism of genetic exchange between cells. *Nat. Cell Biol.* **9**, 654–659 (2007).
5. Tian, F. et al. Protein analysis of extracellular vesicles to monitor and predict therapeutic response in metastatic breast cancer. *Nat. Commun.* **12**, 2536 (2021).
6. Cheng, L. et al. Prognostic serum miRNA biomarkers associated with Alzheimer's disease shows concordance with neuropsychological and neuroimaging assessment. *Mol. Psychiatry* **20**, 1188–1196 (2015).
7. Liang, X. et al. Photothermal cancer immunotherapy by erythrocyte membrane-coated black phosphorus formulation. *J. Control. Release* **296**, 150–161 (2019).
8. Jiang, Q. et al. Erythrocyte–cancer hybrid membrane-camouflaged melanin nanoparticles for enhancing photothermal therapy efficacy in tumors. *Biomaterials* **192**, 292–308 (2019).
9. Duan, X. et al. A new subtype of artificial cell-derived vesicles from dental pulp stem cells with the bioequivalence and higher acquisition efficiency compared to extracellular vesicles. *J. Extracell. Vesicles* **13**, e12473 (2024).
10. Sadeghi, S., Tehrani, F. R., Tahmasebi, S., Shafiee, A. & Hashemi, S. M. Exosome engineering in cell therapy and drug delivery. *Inflammopharmacology* **31**, 145–169 (2023).
11. Liu, J. et al. The biology, function, and applications of exosomes in cancer. *Acta Pharm. Sin. B* **11**, 2783–2797 (2021).
12. Brittle, E. E. & Waters, M. G. Cell biology. ER-to-Golgi traffic—this bud's for you. *Science* **289**, 403–404 (2000).
13. Takamori, S. et al. Molecular anatomy of a trafficking organelle. *Cell* **127**, 831–846 (2006).
14. Bauerfeind, R. & Huttner, W. B. Biogenesis of constitutive secretory vesicles, secretory granules and synaptic vesicles. *Curr. Opin. Cell Biol.* **5**, 628–635 (1993).
15. Yoshihisa, T., Barlowe, C. & Schekman, R. Requirement for a GTPase-activating protein in vesicle budding from the endoplasmic reticulum. *Science* **259**, 1466–1468 (1993).
16. Bonifacino, J. S. & Glick, B. S. The mechanisms of vesicle budding and fusion. *Cell* **116**, 153–166 (2004).
17. Rothman, J. E. The protein machinery of vesicle budding and fusion. *Protein Sci.* **5**, 185–194 (1996).
18. Barlowe, C. et al. COPII: a membrane coat formed by Sec proteins that drive vesicle budding from the endoplasmic reticulum. *Cell* **77**, 895–907 (1994).
19. Gong, B. et al. A Golgi-derived vesicle potentiates PtdIns4P to PtdIns3P conversion for endosome fission. *Nat. Cell Biol.* **23**, 782–795 (2021).
20. Chi, R. J., Harrison, M. S. & Burd, C. G. Biogenesis of endosome-derived transport carriers. *Cell. Mol. Life Sci.* **72**, 3441–3455 (2015).
21. Matsuoka, K. et al. COPII-coated vesicle formation reconstituted with purified coat proteins and chemically defined liposomes. *Cell* **93**, 263–275 (1998).
22. Kaksonen, M. & Roux, A. Mechanisms of clathrin-mediated endocytosis. *Nat. Rev. Mol. Cell Biol.* **19**, 313–326 (2018).
23. Spang, A. On vesicle formation and tethering in the ER–Golgi shuttle. *Curr. Opin. Cell Biol.* **21**, 531–536 (2009).
24. Zhao, J. et al. Membrane localized GbTMEM214s participate in modulating cotton resistance to *Verticillium* wilt. *Plants* **11**, 2342 (2022).
25. Brambilla, D. et al. EV separation: release of intact extracellular vesicles immunocaptured on magnetic particles. *Anal. Chem.* **93**, 5476–5483 (2021).
26. Tang, Y. et al. Schwann cell-derived extracellular vesicles promote memory impairment associated with chronic neuropathic pain. *J. Neuroinflammation* **21**, 99 (2024).
27. Men, Y. et al. Exosome reporter mice reveal the involvement of exosomes in mediating neuron to astroglia communication in the CNS. *Nat. Commun.* **10**, 4136 (2019).
28. Helms, J. B. & Rothman, J. E. Inhibition by brefeldin A of a Golgi membrane enzyme that catalyses exchange of guanine nucleotide bound to ARF. *Nature* **360**, 352–354 (1992).
29. Théry, C. et al. Minimal information for studies of extracellular vesicles 2018 (MISEV2018): a position statement of the International Society for Extracellular Vesicles and update of the MISEV2014 guidelines. *J. Extracell. Vesicles* **7**, 1535750 (2018).
30. Sahu, B. S. et al. Role of clathrin in dense core vesicle biogenesis. *Mol. Biol. Cell* **28**, 2676–2685 (2017).
31. Yu, M., Yan, W. & Beight, C. Lutein and zeaxanthin isomers protect against light-induced retinopathy via decreasing oxidative and endoplasmic reticulum stress in BALB/cJ mice. *Nutrients* **10**, 842 (2018).
32. Jiang, D. et al. Monomethyl fumarate protects the retina from light-induced retinopathy. *Invest. Ophthalmol. Vis. Sci.* **60**, 1275–1285 (2019).
33. Gharagozloo, M. et al. Complement component 3 from astrocytes mediates retinal ganglion cell loss during neuroinflammation. *Acta Neuropathol.* **142**, 899–915 (2021).
34. Zhuang, X. et al. All-trans retinoic acid attenuates blue light-induced apoptosis of retinal photoreceptors by upregulating MKP-1 expression. *Mol. Neurobiol.* **58**, 4157–4168 (2021).
35. Feng, J. H. et al. Cynaroside protects the blue light-induced retinal degeneration through alleviating apoptosis and inducing autophagy in vitro and in vivo. *Phytomedicine* **88**, 153604 (2021).
36. Lin, Y. H. et al. Retinal protective effect of curcumin metabolite hexahydrocurcumin against blue light-induced RPE damage. *Phytomedicine* **110**, 154606 (2023).

37. Chen, P. et al. Retinal neuron is more sensitive to blue light-induced damage than glia cell due to DNA double-strand breaks. *Cells* **8**, 68 (2019).
38. Pennesi, M. E. et al. Long-term characterization of retinal degeneration in rd1 and rd10 mice using spectral domain optical coherence tomography. *Invest. Ophthalmol. Vis. Sci.* **53**, 4644–4656 (2012).
39. Comitato, A., Sanges, D., Rossi, A., Humphries, M. M. & Marigo, V. Activation of Bax in three models of retinitis pigmentosa. *Invest. Ophthalmol. Vis. Sci.* **55**, 3555–3562 (2014).
40. Bernardo-Colón, A. et al. H105A peptide eye drops promote photoreceptor survival in murine and human models of retinal degeneration. *Commun. Med.* **5**, 81 (2025).
41. Nakanishi, T. et al. Role of endoplasmic reticulum stress in light-induced photoreceptor degeneration in mice. *J. Neurochem.* **125**, 111–124 (2013).
42. Wang, Y., Fang, J., Liu, B., Shao, C. & Shi, Y. Reciprocal regulation of mesenchymal stem cells and immune responses. *Cell Stem Cell* **29**, 1515–1530 (2022).
43. Wang, Q. et al. Chitosan-rapamycin carbon dots alleviate glaucomatous retinal injury by inducing autophagy to promote M2 microglial polarization. *Int. J. Nanomed.* **19**, 2265–2284 (2024).
44. Harder, J. M. et al. Disturbed glucose and pyruvate metabolism in glaucoma with neuroprotection by pyruvate or rapamycin. *Proc. Natl Acad. Sci. USA* **117**, 33619–33627 (2020).
45. Merrill, P. T. et al. Efficacy and safety of intravitreal sirolimus for noninfectious uveitis of the posterior segment: results from the Sirolimus Study Assessing Double-Masked Uveitis Treatment (SAKURA) program. *Ophthalmology* **127**, 1405–1415 (2020).
46. Yang, J. L., Zou, T. D., Yang, F., Yang, Z. L. & Zhang, H. B. Inhibition of mTOR signaling by rapamycin protects photoreceptors from degeneration in rd1 mice. *Zool. Res.* **42**, 482–486 (2021).
47. Zhao, C. et al. mTOR-mediated dedifferentiation of the retinal pigment epithelium initiates photoreceptor degeneration in mice. *J. Clin. Invest.* **121**, 369–383 (2011).
48. Wen, Y. et al. Cell-derived nanovesicles prepared by membrane extrusion are good substitutes for natural extracellular vesicles. *Extracell. Vesicle* **1**, 100004 (2022).
49. Brodsky, F. M. Living with clathrin: its role in intracellular membrane traffic. *Science* **242**, 1396–1402 (1988).
50. Trajkovic, K. et al. Ceramide triggers budding of exosome vesicles into multivesicular endosomes. *Science* **319**, 1244–1247 (2008).
51. Lovisa, F. et al. RNY4 in circulating exosomes of patients with pediatric anaplastic large cell lymphoma: an active player? *Front. Oncol.* **10**, 238 (2020).
52. Driedonks, T. A. P. et al. Y-RNA subtype ratios in plasma extracellular vesicles are cell type- specific and are candidate biomarkers for inflammatory diseases. *J. Extracell. Vesicles* **9**, 1764213 (2020).
53. Kwon, S., Yoo, K. H., Sym, S. J. & Khang, D. Mesenchymal stem cell therapy assisted by nanotechnology: a possible combinational treatment for brain tumor and central nerve regeneration. *Int. J. Nanomed.* **14**, 5925–5942 (2019).
54. Kaminska, A., Radoszkiewicz, K., Rybkowska, P., Wedzinska, A. & Sarnowska, A. Interaction of neural stem cells (NSCs) and mesenchymal stem cells (MSCs) as a promising approach in brain study and nerve regeneration. *Cells* **11**, 1464 (2022).
55. Wang, D. et al. The regulation of the Treg/Th17 balance by mesenchymal stem cells in human systemic lupus erythematosus. *Cell. Mol. Immunol.* **14**, 423–431 (2017).
56. Shi, Y. et al. Immunoregulatory mechanisms of mesenchymal stem and stromal cells in inflammatory diseases. *Nat. Rev. Nephrol.* **14**, 493–507 (2018).
57. Simunovic, M., Evergren, E., Callan-Jones, A. & Bassereau, P. Curving cells inside and out: roles of BAR domain proteins in membrane shaping and its cellular implications. *Annu. Rev. Cell. Dev. Biol.* **35**, 111–129 (2019).
58. Xu, J. & Huang, X. Lipid metabolism at membrane contacts: dynamics and functions beyond lipid homeostasis. *Front. Cell Dev. Biol.* **8**, 615856 (2020).
59. Zhu, C., Das, S. L. & Baumgart, T. Nonlinear sorting, curvature generation, and crowding of endophilin N-BAR on tubular membranes. *Biophys. J.* **102**, 1837–1845 (2012).
60. Clarke, J. A., Heron, A. J., Seddon, J. M. & Law, R. V. The diversity of the liquid ordered (Lo) phase of phosphatidylcholine/cholesterol membranes: a variable temperature multinuclear solid-state NMR and X-ray diffraction study. *Biophys. J.* **90**, 2383–2393 (2006).
61. Mills, T. T. et al. Order parameters and areas in fluid-phase oriented lipid membranes using wide angle X-ray scattering. *Biophys. J.* **95**, 669–681 (2008).
62. Le, N. T. T. et al. Soy lecithin-derived liposomal delivery systems: surface modification and current applications. *Int. J. Mol. Sci.* **20**, 4706 (2019).
63. Liang, M., Guo, M., Saw, P. E. & Yao, Y. Fully natural lecithin encapsulated nano-resveratrol for anti-cancer therapy. *Int. J. Nanomed.* **17**, 2069–2078 (2022).
64. Wünsch, A., Mulac, D. & Langer, K. Lipoprotein imitating nanoparticles: lecithin coating binds ApoE and mediates non-lysosomal uptake leading to transcytosis over the blood–brain barrier. *Int. J. Pharm.* **589**, 119821 (2020).
65. MacCuaig, W. M. et al. Active targeting significantly outperforms nanoparticle size in facilitating tumor-specific uptake in orthotopic pancreatic cancer. *ACS Appl. Mater. Interfaces* **13**, 49614–49630 (2021).
66. Chithrani, B. D., Ghazani, A. A. & Chan, W. C. Determining the size and shape dependence of gold nanoparticle uptake into mammalian cells. *Nano Lett.* **6**, 662–668 (2006).
67. Enea, M. et al. A multiparametric study of gold nanoparticles cytotoxicity, internalization and permeability using an in vitro model of blood–brain barrier. Influence of size, shape and capping agent. *Nanotoxicology* **13**, 990–1004 (2019).
68. Jiang, W., Kim, B. Y., Rutka, J. T. & Chan, W. C. Nanoparticle-mediated cellular response is size-dependent. *Nat. Nanotechnol.* **3**, 145–150 (2008).
69. Zhang, H. et al. Identification of distinct nanoparticles and subsets of extracellular vesicles by asymmetric flow field-flow fractionation. *Nat. Cell Biol.* **20**, 332–343 (2018).
70. Yang, L. P., Wu, L. M., Guo, X. J., Li, Y. & Tso, M. O. Endoplasmic reticulum stress is activated in light-induced retinal degeneration. *J. Neurosci. Res.* **86**, 910–919 (2008).
71. Song, J. Y. et al. Suppressing endoplasmic reticulum stress-related autophagy attenuates retinal light injury. *Aging* **12**, 16579–16596 (2020).
72. Deng, C. L. et al. Photoreceptor protection by mesenchymal stem cell transplantation identifies exosomal MiR-21 as a therapeutic for retinal degeneration. *Cell Death Differ.* **28**, 1041–1061 (2021).
73. Li, Y., Li, T., Li, J. Z. & Wu, Q. S. (2R, 3S)-Pinobanksin-3-cinnamate ameliorates photoreceptor degeneration in Pde6^{rd10} mice. *Cutan. Ocul. Toxicol.* **36**, 273–277 (2017).
74. Kang, K. et al. Carnosic acid slows photoreceptor degeneration in the Pde6b^{rd10} mouse model of retinitis pigmentosa. *Sci. Rep.* **6**, 22632 (2016).
75. Wang, T. & Chen, J. Induction of the unfolded protein response by constitutive G-protein signaling in rod photoreceptor cells. *J. Biol. Chem.* **289**, 29310–29321 (2014).
76. Dong, X. et al. Exosome-mediated delivery of an anti-angiogenic peptide inhibits pathological retinal angiogenesis. *Theranostics* **11**, 5107–5126 (2021).
77. Zhang, M. et al. A translocation pathway for vesicle-mediated unconventional protein secretion. *Cell* **181**, 637–652.e15 (2020).
78. Sochacki, K. A. et al. Imaging the post-fusion release and capture of a vesicle membrane protein. *Nat. Commun.* **3**, 1154 (2012).

79. L, P. K. et al. The mesenchymal stem cell secretome: a new paradigm towards cell-free therapeutic mode in regenerative medicine. *Cytokine Growth Factor Rev.* **46**, 1–9 (2019).
80. Liu, H. et al. Analysis of extracellular vesicle DNA at the single-vesicle level by nano-flow cytometry. *J. Extracell. Vesicles* **11**, e12206 (2022).
81. Dunn, K. C., Aotaki-Keen, A. E., Putkey, F. R. & Hjelmeland, L. M. ARPE-19, a human retinal pigment epithelial cell line with differentiated properties. *Exp. Eye Res.* **62**, 155–169 (1996).
82. Xiao, J. et al. Proteomic analysis of plasma sEVs reveals that TNFAIP8 is a new biomarker of cell proliferation in diabetic retinopathy. *J. Proteome Res.* **20**, 1770–1782 (2021).
83. Fan, R. et al. Enhanced therapeutic effect of PEDF-loaded mesenchymal stem cell-derived small extracellular vesicles against oxygen-induced retinopathy through increased stability and penetrability of PEDF. *J. Nanobiotechnology* **21**, 327 (2023).
84. Zhao, W. et al. Sparse deconvolution improves the resolution of live-cell super-resolution fluorescence microscopy. *Nat. Biotechnol.* **40**, 606–617 (2022).
85. Huang, X. et al. Fast, long-term, super-resolution imaging with Hessian structured illumination microscopy. *Nat. Biotechnol.* **36**, 451–459 (2018).
86. Wu, L. et al. Comprehensive profiling of extracellular vesicles in uveitis and scleritis enables biomarker discovery and mechanism exploration. *J. Transl. Med.* **21**, 388 (2023).
87. Fu, Y. et al. The evolution of lipidomics during oil accumulation of *Plukenetia volubilis* seeds. *Plants* **13**, 2193 (2024).
88. Su, L. et al. Mechanism of action of platinum nanoparticles implying from antioxidant to metabolic programming in light-induced retinal degeneration model. *Redox Biol.* **65**, 102836 (2023).
89. Fischer, M. D. et al. Noninvasive, in vivo assessment of mouse retinal structure using optical coherence tomography. *PLoS ONE* **4**, e7507 (2009).
90. Yang, F. et al. TNFAIP8 overexpression aggravates retinal pathophysiological features of diabetic retinopathy. *Exp. Eye Res.* **234**, 109572 (2023).
91. Xu, X. et al. Degeneration of cone photoreceptors induced by expression of the Mas1 protooncogene. *Exp. Neurol.* **163**, 207–219 (2000).
92. Osada, H. et al. Neuroprotective effect of bilberry extract in a murine model of photo-stressed retina. *PLoS ONE* **12**, e0178627 (2017).
93. Li, H. et al. Therapeutic effect of rapamycin-loaded small extracellular vesicles derived from mesenchymal stem cells on experimental autoimmune uveitis. *Front. Immunol.* **13**, 864956 (2022).
94. Jiang, X. et al. Strategic delivery of rapamycin and ranibizumab with intravitreal hydrogel depot disrupts multipathway-driven angiogenesis loop for boosted wAMD therapy. *J. Control. Release* **377**, 239–255 (2025).
95. Bohrey, S., Chourasiya, V. & Pandey, A. Polymeric nanoparticles containing diazepam: preparation, optimization, characterization, in-vitro drug release and release kinetic study. *Nano Converg.* **3**, 3 (2016).
96. Zhang, H. Source Data for MSC-sIVs and MSC-sEVs Study. *figshare* https://doi.org/10.6084/m9.figshare.30226015 (2025).

Acknowledgements

This research was supported by the National Natural Science Foundation of China (82371044, X.Z.; 82171042, X.Z.; 82471106, X.L.) and the Tianjin Key Medical Discipline Construction Project (TJYXZDXK-3-004A-2, X.L. and X.Z.); the Tianjin Health Commission Key Discipline Special Project (TJWJ2023XK009, X.Z.); the Tianjin Medical University 'Clinical Talent Training 123 Climbing Plan' (X.Z.); and the Postdoctoral Talent Project of Tianjin Medical University Eye Hospital (H.Z.). We thank S. Zhang (Nankai University) for helpful suggestions; L. Yu (Tsinghua University) for valuable and insightful suggestions; L. Chen (Peking University) for conducting HIS-SIM imaging; L. Wei (Second Affiliated Hospital, Guangzhou Medical University) for helpful and constructive advice on the manuscript; H. Xu (Southwest Hospital/Southwest Eye Hospital, Third Military Medical University (Army Medical University)) for providing the B6.CXB1-Pde6brd10/J mouse; and Beijing Beilai Biotechnology Co., Ltd. for providing the stem cells.

Author contributions

X.Z. conceived the study. X.L. and X.Z. designed the study. H.Z., X.Y., Y.L. and H.Y. carried out the experiments. J.A., F.Y., L.S. and H.Z. processed and analysed data. X.Z., X.L. and H.Z. drafted the manuscript. M.Z. and R.F. conducted animal experiments during the revision phase. All authors read and approved the final version of the manuscript.

Competing interests

Two patent applications related to this work have been filed (ZL 2024 1 0605829.8 and ZL 2024 1 0605857.X). The authors declare no competing interests.

Additional information

Extended data is available for this paper at https://doi.org/10.1038/s41551-025-01596-1.

Supplementary information The online version contains supplementary material available at https://doi.org/10.1038/s41551-025-01596-1.

Correspondence and requests for materials should be addressed to Xiaorong Li or Xiaomin Zhang.

Peer review information *Nature Biomedical Engineering* thanks Carl Randall Harrell, Valeria (A.) Marigo and the other, anonymous, reviewer(s) for their contribution to the peer review of this work. Peer reviewer reports are available.

https://doi.org/10.1038/s41551-025-01596-1

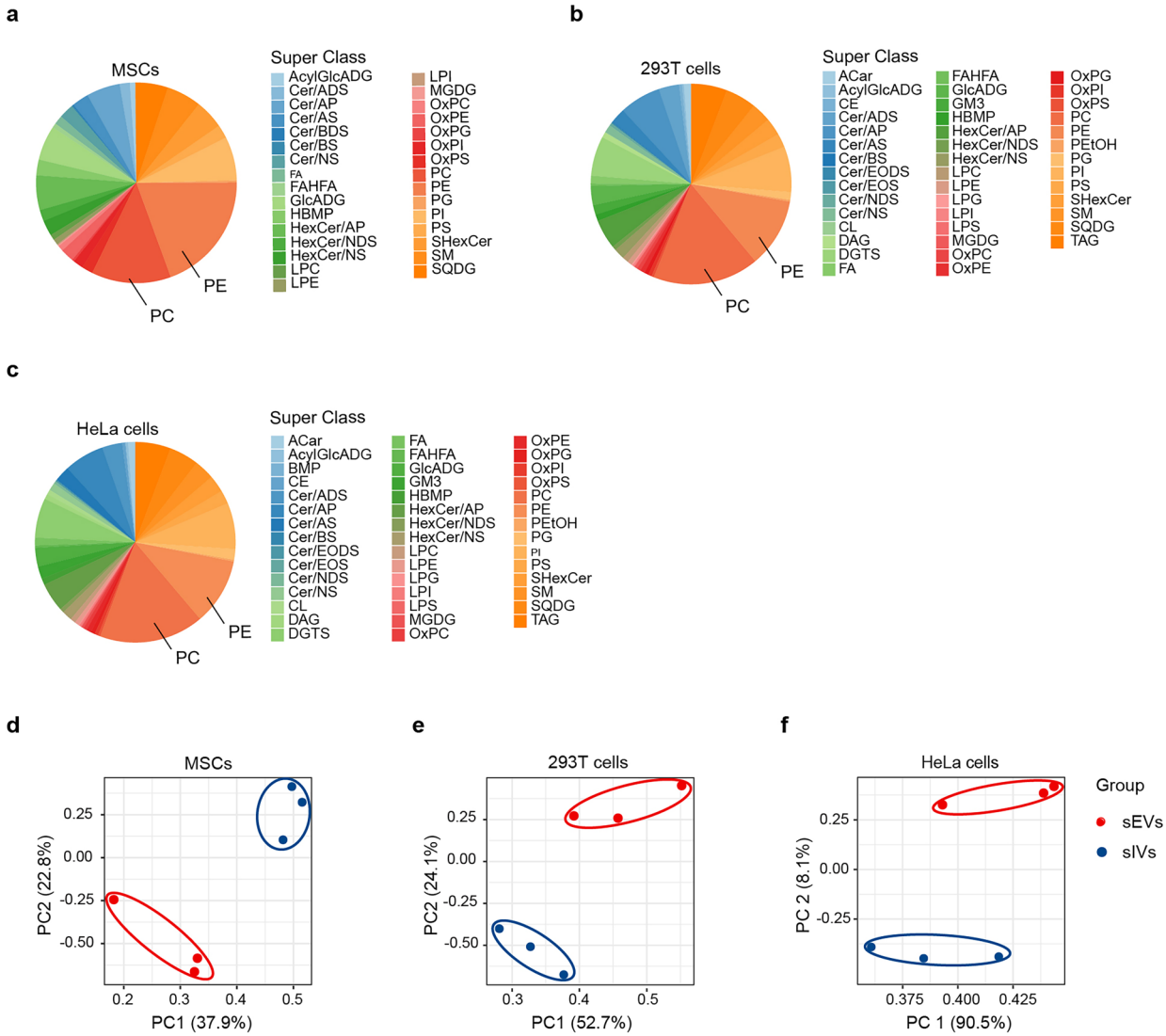

Extended Data Fig. 1 | Differential expression of lipid components in sIVs and sEVs from MSCs, 293 T cells, and HeLa cells. (**a**–**c**) Distribution of lipids categories from MSCs (**a**), 293 T cells (**b**), and HeLa cells (**c**). (**d**–**f**) Principal component analysis of lipids in sEVs and sIVs from MSCs (**d**), 293 T cells (**e**), and HeLa cells (**f**).

https://doi.org/10.1038/s41551-025-01596-1

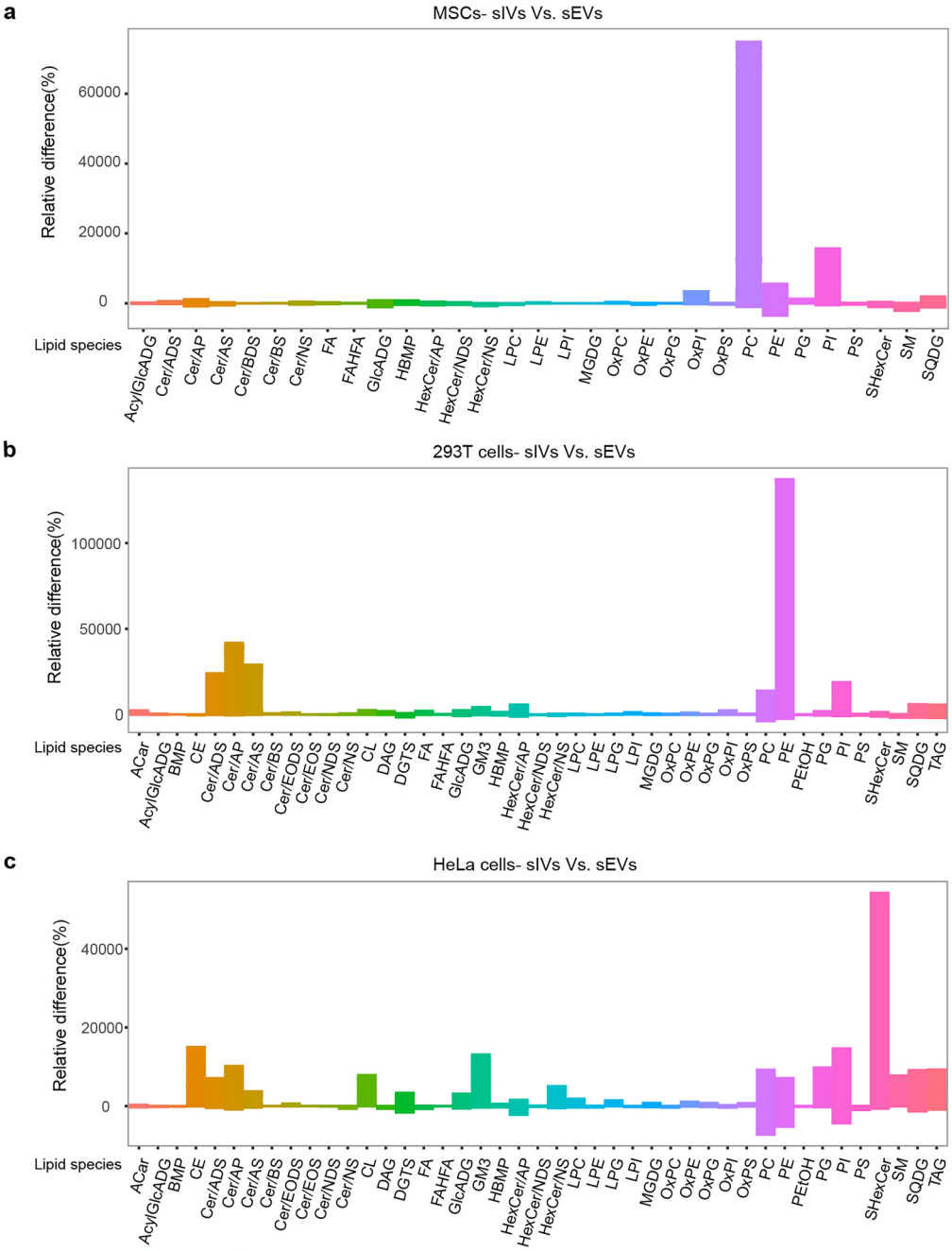

Extended Data Fig. 2 | Column chart of lipid profiles of sIVs and sEVs from MSCs, 293 T cells, and HeLa cells. (**a**–**c**) Lipidomic bar plots depicting changes in metabolite content and lipid classification from MSCs (**a**), 293 T cells (**b**), and HeLa cells (**c**). The vertical axis represents the relative percentage change in lipid content of each substance in the compared groups. A zero-percentage change indicates equal lipid content between the two groups; positive values indicate higher lipid content in the sIV group, while negative values indicate higher content in the sEV group. The horizontal axis shows the lipid classification.

https://doi.org/10.1038/s41551-025-01596-1

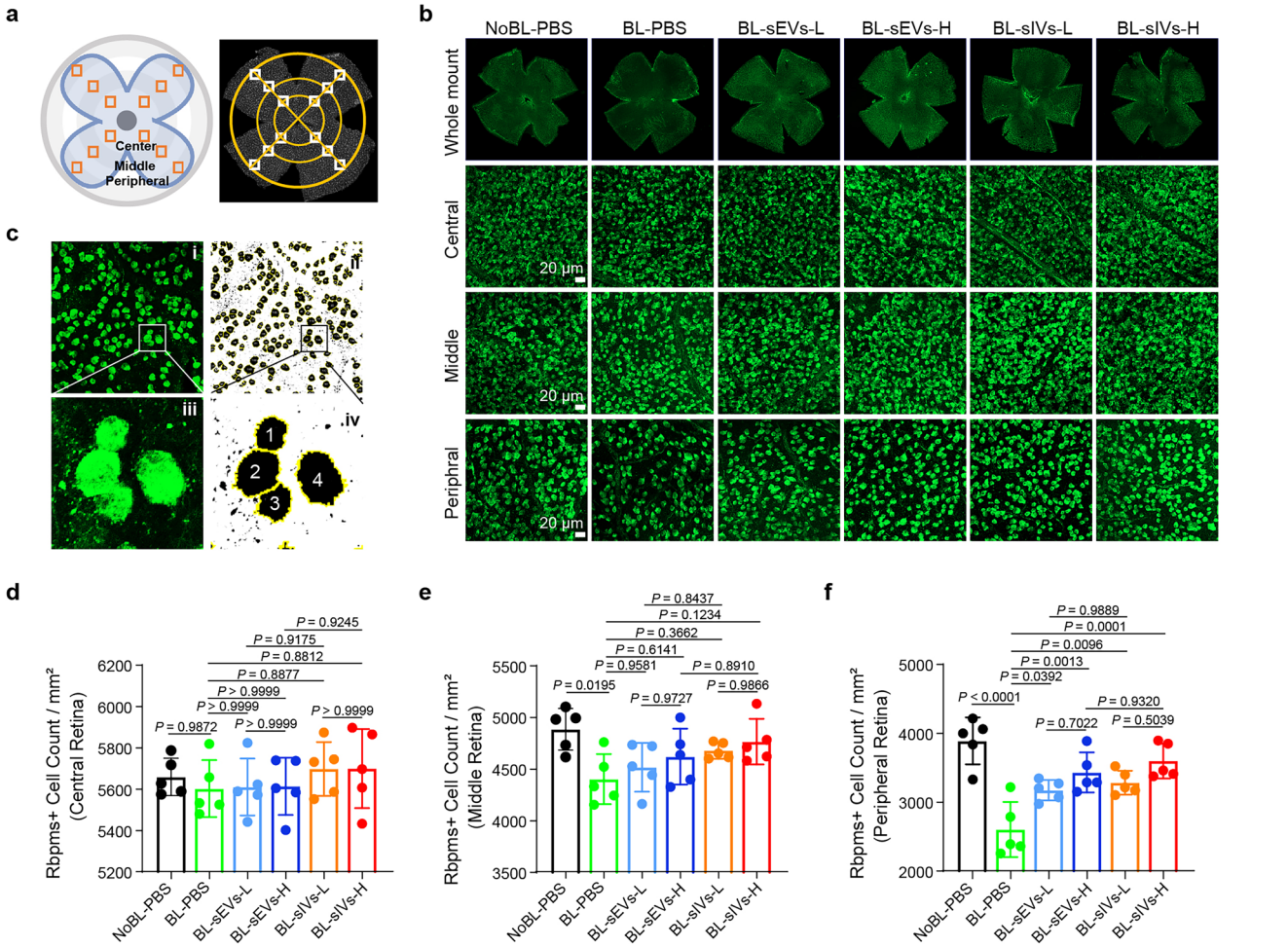

Extended Data Fig. 3 | Protective role of MSC-sIVs and MSC-sEVs on retinal ganglion cells in light-damaged mice. a, Representative flat mount preparation showed three areas: central, middle, and peripheral. Photographs of each area in each arm were taken using a confocal microscope. Shown results reflect at least three independent experiments, all producing similar findings. **b**, Distribution of RBPMS-positive cells in the retina; the green signal represents RBPMS. L: low-dose vesicles (2 μg), H: high-dose vesicles (4 μg). **c**, RBPMS-positive cells were counted using Image J software and analyzed. (**d**–**f**) Quantitative analysis of RBPMS-positive cells in the central retina (**d**), middle retina (**e**), and peripheral retina (**f**) ($n = 5$ biologically independent samples). Data in **d, e, f** are presented as mean ± s.e.m. and are compared by one-way ANOVA.

https://doi.org/10.1038/s41551-025-01596-1

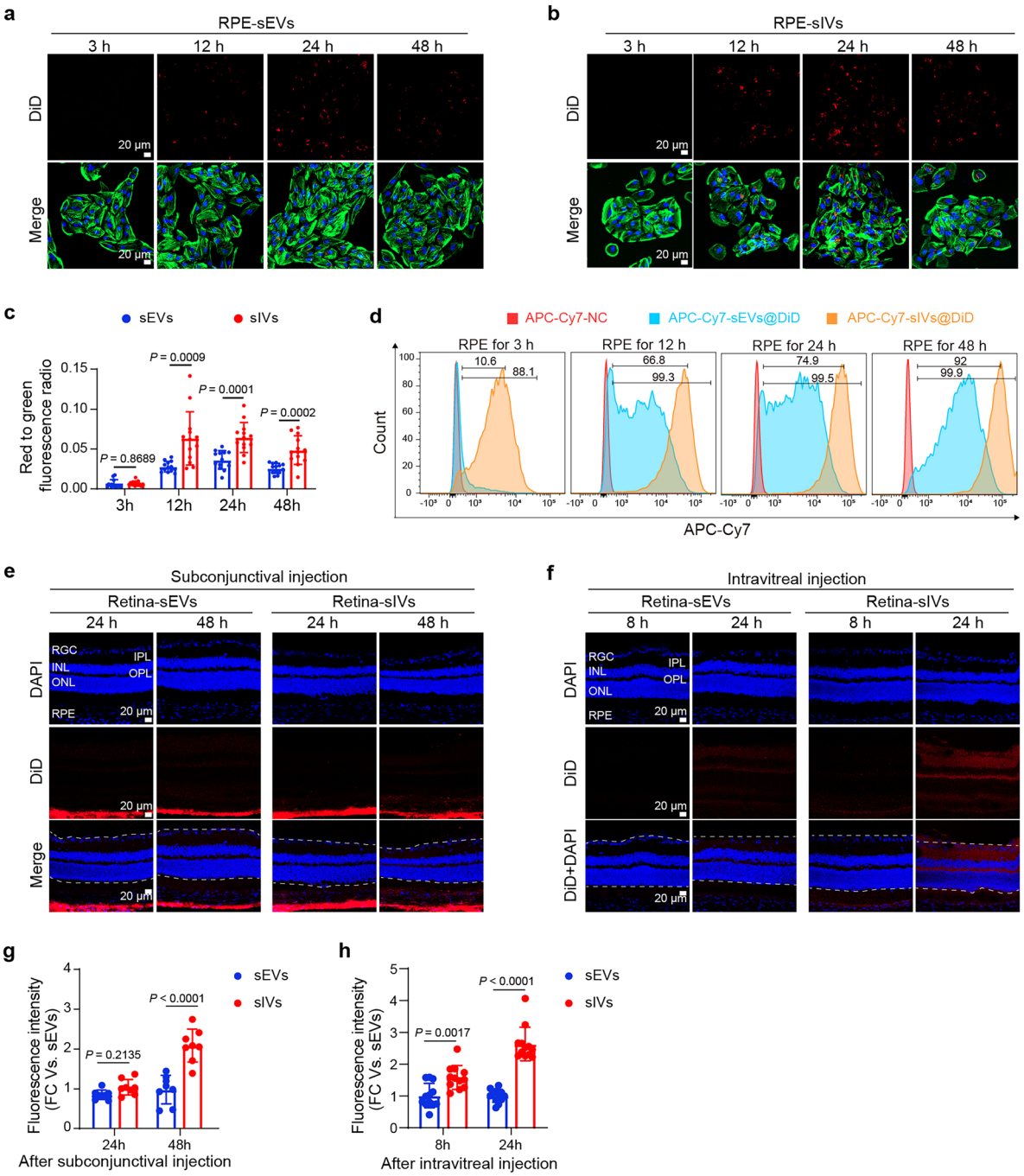

Extended Data Fig. 4 | Enhanced cell and tissue uptake of MSC-derived sIVs. (**a, b**) DiD-labeled sEVs (**a**) and sIVs (**b**) were co-cultured with RPE cells for 3, 12, 24, and 48 h. The green, red, and blue signals indicate phalloidin staining, DiD, and DAPI staining, respectively. Scale bars: 20 μm. (**c**) Cellular uptake of sEVs and sIVs was quantified by measuring the fluorescence intensity ($n = 13$ biologically independent samples). **d**, Flow cytometry was employed to analyze RPE cells incubated with sEVs and sIVs over varying time intervals. NC: DiD dye without vesicles, but subjected to the same staining procedure as the vesicle samples. **e-f**, Distribution of sEVs and sIVs labeled with DiD in the retina following subconjunctival injection (**e**) and intravitreal injection (**f**). The red and blue signals indicate DiD and DAPI staining, respectively. Scale bars: 20 μm. **g-h**, Quantification of the retina fluorescence intensity in the subconjunctival injection group (**g**) ($n = 8$ biologically independent samples) and intravitreal injection group (**h**) ($n = 12$ biologically independent samples). The dashed lines delineate the region used for fluorescence analysis. Representative images are shown; similar results were obtained in at least three independent experiments. Data in **c, g, h** are presented as mean ± s.e.m. and are compared by two-tailed unpaired Student's *t*-test.

https://doi.org/10.1038/s41551-025-01596-1

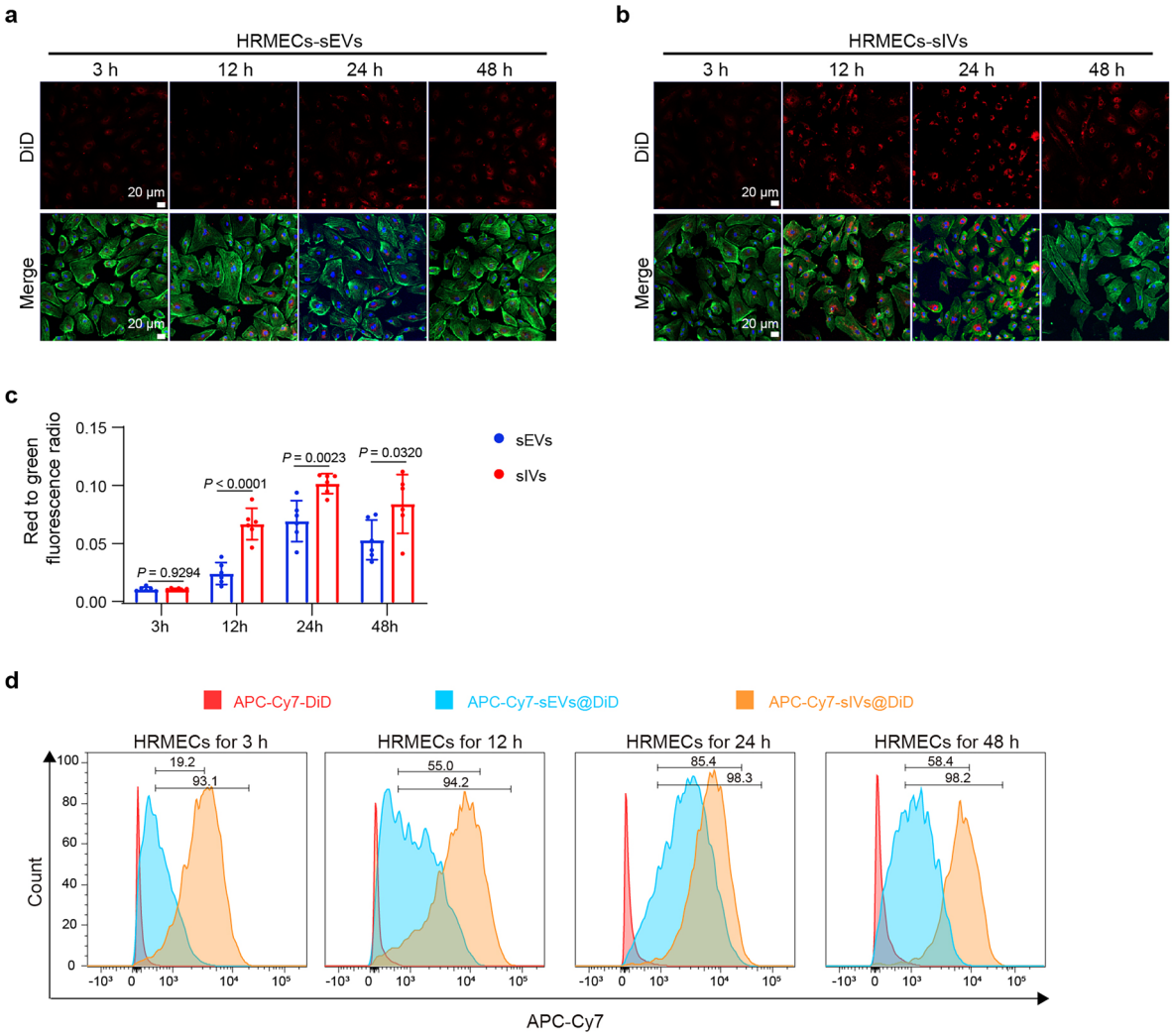

Extended Data Fig. 5 | Enhanced HRMEC uptake of MSC-derived sIVs. (**a,b**) DiD-labeled sEVs (**a**) and sIVs (**b**) were co-cultured with HRMECs for 3 h, 12 h, 24 h, and 48 h. The green signal represents phalloidin staining, the red signal represents DiD, and the blue signal represents DAPI staining. **c**, Quantification of cellular uptake of sEVs and sIVs by measuring fluorescence intensity ($n = 6$ biologically independent samples). Data are presented as mean ± s.e.m. and are compared by two-tailed unpaired Student's *t*-test. **d**, Flow cytometry was employed to analyze HRMECs incubated with sEVs and sIVs over varying time intervals. NC: DiD dye without vesicles, but subjected to the same staining procedure as the vesicle samples. Representative images are shown; similar results were obtained in at least three independent experiments.

nature portfolio

Corresponding author(s): Xiaorong Li, Xiaomin Zhang

Last updated by author(s): Sep 27, 2025

Reporting Summary

Nature Portfolio wishes to improve the reproducibility of the work that we publish. This form provides structure for consistency and transparency in reporting. For further information on Nature Portfolio policies, see our Editorial Policies and the Editorial Policy Checklist.

Statistics

For all statistical analyses, confirm that the following items are present in the figure legend, table legend, main text, or Methods section.

n/a	Confirmed	
☐	☒	The exact sample size (*n*) for each experimental group/condition, given as a discrete number and unit of measurement
☐	☒	A statement on whether measurements were taken from distinct samples or whether the same sample was measured repeatedly
☐	☒	The statistical test(s) used AND whether they are one- or two-sided *Only common tests should be described solely by name; describe more complex techniques in the Methods section.*
☒	☐	A description of all covariates tested
☐	☒	A description of any assumptions or corrections, such as tests of normality and adjustment for multiple comparisons
☐	☐	A full description of the statistical parameters including central tendency (e.g. means) or other basic estimates (e.g. regression coefficient) AND variation (e.g. standard deviation) or associated estimates of uncertainty (e.g. confidence intervals)
☐	☒	For null hypothesis testing, the test statistic (e.g. *F*, *t*, *r*) with confidence intervals, effect sizes, degrees of freedom and *P* value noted *Give P values as exact values whenever suitable.*
☒	☐	For Bayesian analysis, information on the choice of priors and Markov chain Monte Carlo settings
☒	☐	For hierarchical and complex designs, identification of the appropriate level for tests and full reporting of outcomes
☐	☒	Estimates of effect sizes (e.g. Cohen's *d*, Pearson's *r*), indicating how they were calculated

Our web collection on statistics for biologists contains articles on many of the points above.

Software and code

Policy information about availability of computer code

Data collection	Densitometric data were quantified using ImageJ (1.8.0_172) and standardized based on the expression of the internal control. NTA results were examined using NTA software (NTA 3.3 Dev Build 3.3.104) in an automated manner. A QE mass spectrometer was employed as it uses a data-dependent acquisition mode to capture MS/MS spectra under acquisition software control (Xcalibur 4.0.27, Thermo). Flow cytometry data were collected using a FACSVerse flow cytometer (BD Biosciences, USA).
Data analysis	Statistical analyses were carried out via GraphPad Prism 9.0.0. Flow cytometry data were analyzed using flow cytometry software (FlowJo 10.8.1,, USA).

For manuscripts utilizing custom algorithms or software that are central to the research but not yet described in published literature, software must be made available to editors and reviewers. We strongly encourage code deposition in a community repository (e.g. GitHub). See the Nature Portfolio guidelines for submitting code & software for further information.

Data

Policy information about availability of data

All manuscripts must include a data availability statement. This statement should provide the following information, where applicable:

- Accession codes, unique identifiers, or web links for publicly available datasets
- A description of any restrictions on data availability
- For clinical datasets or third party data, please ensure that the statement adheres to our policy

The primary data underlying the findings of this study are included in the article and its Supplementary Information. The mass spectrometry proteomics data have been deposited to the ProteomeXchange Consortium via the iProX partner repository with the dataset identifier PXD051827. The primary vesicle sequencing data from this study have been deposited in the Genome Sequence Archive (GSA-Human: HRA007464). All the metabolic data are deposited in the MetaboLights platform (MTBLS12923). The RNA-sequencing data for rd10 mice and blue-light-damaged mice are available at the NCBI GEO under accession GSE309223 and GSE309258. The source data for the figures are provided in the Supplementary Information and have also been deposited at figshare: 10.6084/m9.figshare.30226015. Details of all commercially obtained reagents are provided in the Supplementary Key Resources Table.

Research involving human participants, their data, or biological material

Policy information about studies with human participants or human data. See also policy information about sex, gender (identity/presentation), and sexual orientation and race, ethnicity and racism.

Reporting on sex and gender	This study does not involve clinical or population research.
Reporting on race, ethnicity, or other socially relevant groupings	This study does not involve clinical or population research.
Population characteristics	This study does not involve clinical or population research.
Recruitment	This study does not involve clinical or population research.
Ethics oversight	This study does not involve clinical or population research.

Note that full information on the approval of the study protocol must also be provided in the manuscript.

Field-specific reporting

Please select the one below that is the best fit for your research. If you are not sure, read the appropriate sections before making your selection.

☒ Life sciences ☐ Behavioural & social sciences ☐ Ecological, evolutionary & environmental sciences

For a reference copy of the document with all sections, see nature.com/documents/nr-reporting-summary-flat.pdf

Life sciences study design

All studies must disclose on these points even when the disclosure is negative.

Sample size	We performed a power analysis to ensure that the sample size was sufficient to detect biologically relevant effects with a statistical power of 80% and a significance level of 0.05. The detailed formula used for the calculation is presented in the main text. The expected effect size (Δ) and estimated standard deviation (σ) were derived from preliminary experiments and relevant literature. We included a minimum of three biological replicates or three animals per group to calculate means, standard deviations, and conduct statistical analyses.
Data exclusions	No data excluded.
Replication	We have provided a detailed report on the steps of conducting the experiment for any other researchers to replicate. For relevant experiments, we report pooled results from multiple experiments or the data shown correspond to one representative experiment of at least 3 experiments. All reported experiments were successfully replicated, and the results were consistent across independent biological replicates.
Randomization	In this study, samples were allocated into experimental groups using a randomization process, which involved employing a random number generator to ensure equal chances for each subject to be assigned to a specific group.
Blinding	In this study, the investigators were blinded to group allocation during both data collection and analysis to minimize the risk of bias and ensure objective assessment of the outcomes.

Reporting for specific materials, systems and methods

We require information from authors about some types of materials, experimental systems and methods used in many studies. Here, indicate whether each material, system or method listed is relevant to your study. If you are not sure if a list item applies to your research, read the appropriate section before selecting a response.

Materials & experimental systems

n/a	Involved in the study
☐	☒ Antibodies
☐	☒ Eukaryotic cell lines
☒	☐ Palaeontology and archaeology
☐	☒ Animals and other organisms
☒	☐ Clinical data
☒	☐ Dual use research of concern
☒	☐ Plants

Methods

n/a	Involved in the study
☒	☐ ChIP-seq
☐	☒ Flow cytometry
☒	☐ MRI-based neuroimaging

Antibodies

Antibodies used

Western blot
Rabbit monoclonal anti-Alix (ab186429; Abcam; 1:1000 dilution)
Rabbit polyclonal anti-HSP70（10995;Proteintech; 1:1000 dilution）
Rabbit monoclonal anti-CD81（ab109201;Abcam; 1:500 dilution）
Rabbit polyclonal anti-CD63（ab216130;Abcam; 1:1000 dilution）
Rabbit polyclonal anti-TSG101（28283;Proteintech; 1:1000 dilution）
Rabbit polyclonal anti-TMEM214（20125;Proteintech; 1:1000 dilution）
Mouse monoclonal anti-Rhodopsin（ab5417;Abcam; 1:10000 dilution）
Rabbit polyclonal anti-GFAP（ab7260;Abcam; 1:5000 dilution）
Rabbit polyclonal anti-Cleaved-Caspase3（9661;Cell Signaling Technology; 1:1000 dilution）
Rabbit polyclonal anti-Caspase3（9662;Cell Signaling Technology; 1:4000 dilution）
Rabbit monoclonal anti-β-actin?4970;Cell Signaling Technology; 1:10000 dilution?
Rabbit monoclonal anti-BCL2（3498;Cell Signaling Technology; 1:1000 dilution）
Mouse monoclonal anti- PSD95（ab238135;Abcam; 1:2000 dilution）
Rabbit polyclonal anti-GRP78（ab21685;Abcam; 1:1000 dilution）
Rabbit monoclonal anti-IRE1α（3294;Cell Signaling Technology; 1:1000 dilution?
Rabbit polyclonal anti-Phospho-PERK（HY-P80845;Med Chem Express; 1:1000 dilution）
Rabbit monoclonal anti-PERK（HY-P80781;Med Chem Express; 1:1000 dilution）
Rabbit monoclonal anti-ATF6（65880;Cell Signaling Technology; 1:1000 dilution）
Mouse monoclonal anti-CHOP（2895;Cell Signaling Technology; 1:1000 dilution）
Rabbit monoclonal anti-Phospho-eIF2α（3398;Cell Signaling Technology; 1:1000 dilution?
Rabbit monoclonal anti-Phospho-eIF2α（5324;Cell Signaling Technology; 1:1000 dilution?
Rabbit monoclonal anti-Bax（ab32503;Abcam; 1:1000 dilution）
Immunofluorescence staining
Rabbit polyclonal anti-Rbpms （ABN1376;Millipore; 1:100 dilution）
Rabbit monoclonal anti-IBA1（ab178847;Abcam; 1:100 dilution）
Mouse monoclonal anti-Rhodopsin（ab5417;Abcam; 1:10000 dilution）
Rabbit polyclonal anti-GFAP（ab7260;Abcam; 1:5000 dilution）
Mouse monoclonal anti- PSD95（ab238135;Abcam; 1:2000 dilution）
Rabbit monoclonal anti-EEA1（ab109110;Abcam; 1:1000 dilution）
Rabbit monoclonal anti-Rab7（ab137029;Abcam; 1:1000 dilution）
Rabbit monoclonal anti-Phospho-mTOR （5536;Cell Signaling Technology; 1:1000 dilution）
Rabbit monoclonal anti-mTOR （2983;Cell Signaling Technology; 1:1000 dilution）

Validation

Rabbit monoclonal anti-Alix (ab186429; Abcam)
https://www.abcam.cn/products/primary-antibodies/alix-antibody-epr15314-n-terminal-ab186429.html
Rabbit monoclonal anti-Phospho-mTOR （5536;Cell Signaling Technology）
https://www.cellsignal.com/products/primary-antibodies/phospho-mtor-ser2448-d9c2-xp-rabbit-mab/5536
Rabbit monoclonal anti-mTOR （2983;Cell Signaling Technology）
https://www.cellsignal.com/products/primary-antibodies/mtor-7c10-rabbit-mab/2983
Rabbit monoclonal anti-EEA1（ab109110;Abcam; 1:1000 dilution）
https://www.abcam.cn/products/primary-antibodies/eea1-antibody-epr4245-early-endosome-marker-ab109110.html
Rabbit monoclonal anti-Rab7（ab137029;Abcam; 1:1000 dilution）
https://www.abcam.cn/products/primary-antibodies/rab7-antibody-epr7589-ab137029.html
Rabbit polyclonal anti-HSP70（10995）Proteintech）
https://www.ptgcn.com/Products/HSPA1A-Antibody-10995-1-AP.htm
Rabbit monoclonal anti-CD81（ab109201）Abcam）
https://www.abcam.cn/products/primary-antibodies/cd81-antibody-epr4244-ab109201.html
Rabbit polyclonal anti-CD63（ab216130）Abcam）
https://www.abcam.cn/products/primary-antibodies/cd63-antibody-late-endosome-marker-ab216130.html
Rabbit polyclonal anti-TSG101（28283）Proteintech）
https://www.thermofisher.cn/cn/zh/antibody/product/TSG101-Antibody-Polyclonal/28283-1-AP
Rabbit polyclonal anti-TMEM214（20125）Proteintech）
https://www.ptgcn.com/products/TMEM214-Antibody-20125-1-AP.htm
Mouse monoclonal anti-Rhodopsin（ab5417）Abcam）

https://www.abcam.cn/products/primary-antibodies/rhodopsin-antibody-1d4-ab5417.html
Rabbit polyclonal anti-Rbpms （ABN1376）Millipore）
https://www.sigmaaldrich.cn/CN/zh/product/mm/abn1376
Rabbit polyclonal anti-GFAP（ab7260）Abcam）
https://www.abcam.cn/products/primary-antibodies/gfap-antibody-ab7260.html
Rabbit polyclonal anti-Cleaved-Caspase3（9661）Cell Signaling Technology）
https://www.cellsignal.cn/products/primary-antibodies/cleaved-caspase-3-asp175-antibody/9661
Rabbit polyclonal anti-Caspase3（9662）Cell Signaling Technology）
https://www.cellsignal.com/products/primary-antibodies/caspase-3-antibody/9662
Rabbit monoclonal anti-Bax（ab32503）Abcam）
https://www.abcam.cn/products/primary-antibodies/bax-antibody-e63-ab32503.html
Rabbit monoclonal anti-β-actin?4970?Cell Signaling Technology?
https://www.cellsignal.cn/products/primary-antibodies/b-actin-13e5-rabbit-mab/4970
Rabbit monoclonal anti-BCL2（3498）Cell Signaling Technology）
https://www.cellsignal.cn/products/primary-antibodies/bcl-2-d17c4-rabbit-mab-mouse-preferred/3498
Rabbit monoclonal anti-IBA1（ab178847）Abcam）
https://www.abcam.cn/products/primary-antibodies/iba1-antibody-epr16589-ab178847.html
Mouse monoclonal anti- PSD95（ab238135）Abcam）
https://www.abcam.cn/products/primary-antibodies/psd95-antibody-epr23124-118-synaptic-marker-ab238135.html
Rabbit polyclonal anti-GRP78（ab21685）Abcam）
https://www.abcam.cn/products/primary-antibodies/grp78-bip-antibody-ab21685.html
Rabbit monoclonal anti-IRE1α（3294?Cell Signaling Technology?
https://www.cellsignal.com/products/primary-antibodies/ire1a-14c10-rabbit-mab/3294
Rabbit polyclonal anti-Phospho-PERK（HY-P80845）Med Chem Express）
https://www.medchemexpress.cn/search.html?q=HY-P80845&ft=&fa=&fp=&type=antibodies
Rabbit monoclonal anti-PERK（HY-P80781）Med Chem Express）
https://www.medchemexpress.cn/antibody/perk-rabbit-mab.html
Rabbit monoclonal anti-ATF6（65880）Cell Signaling Technology）
https://www.cellsignal.com/products/primary-antibodies/atf-6-d4z8v-rabbit-mab/65880
Mouse monoclonal anti-CHOP（2895）Cell Signaling Technology）
https://www.cellsignal.com/products/primary-antibodies/chop-l63f7-mouse-mab/2895
Rabbit monoclonal anti-Phospho-eIF2α（3398?Cell Signaling Technology?
https://www.cellsignal.com/products/primary-antibodies/phospho-eif2a-ser51-d9g8-xp-rabbit-mab/3398
Rabbit monoclonal anti-Phospho-eIF2α（5324?Cell Signaling Technology?
https://www.cellsignal.cn/products/primary-antibodies/eif2a-d7d3-xp-rabbit-mab/5324

Eukaryotic cell lines

Policy information about cell lines and Sex and Gender in Research

Cell line source(s)	The 293T and HeLa cells were purchased from the National Collection of Authenticated Cell Cultures. The human RPE cell line APRE19 was obtained from the American Tissue Culture Collection (ATCC, USA).Primary human retinal microvascular endothelial cells (HRMECs) were acquired from Cell Systems (ACBRI 181) and cultured in Endothelial Cell Medium (ECM, ScienCell, USA).
Authentication	Upon the purchase of cells, the supplier provides phase-contrast microscopic images and an authentication report.
Mycoplasma contamination	All cells were tested and confirmed to be free of mycoplasma.
Commonly misidentified lines (See ICLAC register)	No relevant misidentified lines available.

Animals and other research organisms

Policy information about studies involving animals; ARRIVE guidelines recommended for reporting animal research, and Sex and Gender in Research

Laboratory animals	The BALB/c mice (5–6 weeks, male, weighing 17 ± 1 g) were acquired from SPF (Beijing, China). Professor Haiwei Xu of Southwest Medical University kindly donated rd10 (Pde6brd10) mice. Rd10 mice (male, aged 2 weeks, weight of 5.5 ± 0.5 g) were used. The C57BL/6 J mice (male, aged 2 weeks, weighing 5.5 ± 0.5 g) were sourced from SPF (Beijing, China). All experimental mice were male. The Department of Laboratory Animals maintained normal, pathogen-free housing for the animals, with a 12-hour light/dark cycle and four to five mice per cage. Humidity was regulated at 41–44% to ensure animal welfare. The mice used in this investigation were fed a regular chow diet.
Wild animals	This study did not involved wild animals.
Reporting on sex	Male mice were taken for research to reduce the effects of estrogen in female mice.
Field-collected samples	The study did not involve samples collected from the field.
Ethics oversight	All procedures involving animals were performed in accordance with the ARVO statement and Tianjin Medical University Eye Institute Guidelines for Animal Research (TJYY2022122081).

Note that full information on the approval of the study protocol must also be provided in the manuscript.

Plants

Seed stocks	This study does not involve plants.
Novel plant genotypes	This study does not involve plants.
Authentication	This study does not involve plants.

Flow Cytometry

Plots

Confirm that:

☒ The axis labels state the marker and fluorochrome used (e.g. CD4-FITC).

☒ The axis scales are clearly visible. Include numbers along axes only for bottom left plot of group (a 'group' is an analysis of identical markers).

☒ All plots are contour plots with outliers or pseudocolor plots.

☒ A numerical value for number of cells or percentage (with statistics) is provided.

Methodology

Sample preparation	After washing the cells three times with pre-cooled PBS, the cells were digested with trypsin. Following centrifugation to remove the trypsin, the cells were resuspended in PBS for flow cytometry analysis.
Instrument	FACSVerse flow cytometer (BD Biosciences, USA)
Software	FlowJo(10.8.1)
Cell population abundance	Contaminating debris and doublets were excluded by stringent FSC-A/FSC-H gating. The post-sort purity correlates with the temporal dynamics and functional capacity of cellular exosome internalization. Low-uptake populations (<30% purity) suggest limited endocytic activity, whereas high-uptake populations (>80% purity) indicate robust vesicle engulfment.
Gating strategy	Gate 1: FSC-A vs. SSC-A (Live Cell Selection).Gate 2: APC Channel Histogram (Positive Population Identification)

☒ Tick this box to confirm that a figure exemplifying the gating strategy is provided in the Supplementary Information.